Direct numerical simulations of incompressible multiphase magnetohydrodynamics with phase change

Jie Zhang [a], Ming-Jiu Ni [a,b,*]

[a] *State Key Laboratory for Strength and Vibration of Mechanical Structures, School of Aerospace, Xi'an Jiaotong University, Xi'an, Shaanxi 710049, China*
[b] *School of Engineering Science, University of Chinese Academy of Sciences, Beijing 101408, China*

A R T I C L E   I N F O

A B S T R A C T

A new phase change model has been developed for the simulation of incompressible multiphase magnetohydrodynamics based on the Volume-of-Fluid method. To decrease the pressure oscillations when large density contrasts are present between the liquid phase and the vapor phase, a smooth distribution of sharp mass transfer rate within a narrow region surrounding the interface is adopted, and a ghost-cell approach is used to impose the saturating temperature at the liquid–vapor interface when solving the energy equation. After that, the method has been implemented in an incompressible multiphase magnetohydrodynamics solver developed in our previous work (Zhang and Ni (2014) [3]). Moreover, when computing the electromagnetic fields, a cut-cell approach is implemented to keep the sharpness of the interface, which is treated as an electrically insulating boundary as it translates and deforms with the fluid. The phase change model has been verified for a series of one-dimensional, two-dimensional and three-dimensional problems, while the numerical results agree well with either the theoretical solutions or the experimental data. In particular, by simulating the vapor bubble rising in superheated liquid under nonzero gravity in presence of external magnetic field, the magnetohydrodynamics effect on the vaporization of the rising bubble is investigated and we observe the magnetic fields to suppress the vapor bubble growth during the phase change. At last, both two-dimensional and three-dimensional film boiling simulations are conducted, which show good qualitative agreement with heat transfer correlations, and the vapor bubble is found to elongate along the direction of the magnetic field during its growth, moreover, the time instant for the vapor bubble to detach from the film is also delayed.

1. Introduction

As a contactless method, the magnetic fields are always employed to control the liquid metal flow in the metallurgy processes, for stirring or homogenizing purpose such as injecting the bubbles to refine the melt [1]. Besides, in fusion nuclear reactors, where liquid lithium or lithium–lead are widely used as a breeder and heat remover, the multiphase flows of the liquid metal are always subject to the strong magnetic fields [2], and thus their flow characteristics are greatly

---

* Corresponding author at: School of Engineering Science, University of Chinese Academy of Sciences, Beijing 101408, China.
  E-mail address: mjni@ucas.ac.cn (M.-J. Ni).

affected by the magnetohydrodynamics (MHD, hereafter) effect. For this purpose, a numerical methodology to simulate the incompressible multiphase MHD flows has been proposed in our previous study [3], and the approach is developed as an extension of the open-source software Gerris flow solver [4], which combines the Volume-of-Fluid (VOF, hereafter) method and the adaptive mesh refinement (AMR, hereafter) technique for interface tracking and advancing. In that work, a consistent and conservative scheme [5,6] is introduced to solve the electromagnetic field, including the calculation of the electric potential and the Lorentz force. After that, several direct numerical simulations have been conducted to study the multiphase MHD flows, particularly of the single bubble motion [7–9] and the droplet impacting [10,11] problems under the influence of external magnetic fields.

However, another type of multiphase MHD flows involving the vaporization of the liquid metal still requires further investigation, as to achieve high thermal performance at high power density in the thermonuclear fusion device, in which the MHD effect always suppresses the heat transfer efficiency. As a consequence, the Evaporation of Lithium and Vapor Extraction (EVOLVE) blanket concept uses the vaporization of lithium to remove the blanket thermal power [12,13]. In addition, for the boiling lithium blanket, the evaluation of the impacts of magnetic field on various stable-boiling regimes is also in demand [13]. However, difficult as the experiments are [14–16], comprehensive information of the flow field is hardly obtained due to the opacity of the liquid metal, and moreover, the available experimental results are always inconsistent that no universal conclusion with respect to the influence of the magnetic field is obtained. Alternatively, direct numerical simulations would be an effective method to predict the flow behaviors of the phase change problems under the influence of magnetic fields. However, as far as the author know, none of such numerical methods has been proposed in the available publications.

To develop such a robust and accurate phase change model, the difficulties lie in two aspects. First, the mass transfer only happens in the mixed cells which contain the liquid–vapor interface, leading a discontinuity of the velocity field across the interface, and such singularity of the mass source probably produces numerical instability during solving the velocity–pressure coupling equations in vicinity of the interface, particularly with large density contrasts between the two phases. By using a VOF method, Hardt and Wondra [17] employed a smoothing function to smear the mass flux over 4–5 computational cells surrounding the interface, and then the distribution of the mass transfer rate was again artificially shifted to the liquid or vapor side, by this a very stable performance was obtained although the physical significance was declined. Furthermore, in merit of its ease of implementation, Kunkelmann and Stephane [18] further implemented this numerical scheme into the open source code OpenFOAM and then it was widely used. Magnini et al. [19] used a similar smoothing function to smear the mass source into the neighbor cells and the bubble motions during flow boiling in a microchannel were further investigated. Nevertheless, there are some other researchers trying to implement more sharp schemes to capture the jump conditions across the interface. In particular, the Ghost Fluid method (GFM, hereafter) as introduced for solving the Poisson equation is also used to capture the velocity jump condition during phase change, as shown by Son and Dhir [20], and the group of Tanguy [21–23], the numerical results are proved to be in good agreement with the real physics, however, as far as the authors know, most of the sharp mass transfer schemes are implemented within the level-set method. Moreover with a very different approach, Schlottke and Welgand [24] indicate that by using a mass averaged density together with the corrected velocities at the interface, the spurious oscillations of the pressure in vicinity of the interface would be greatly suppressed, and a similar approach is further adopted by Ma and Bothe [25]. Nevertheless, there are also some other studies [26–30] not mentioning how to deal with the singular problem of the mass source, and no flow instabilities are reported either. For the other difficulty, it comes from the internal boundary condition of the temperature at the interface. If there is no extreme high heat flux during phase change that the liquid–vapor interface is assumed to keep at the saturation temperature as T_{sat}, it could be viewed as a variant type of internal Dirichlet boundary condition. Tsui et al. [31,29] use an implicit interpolation scheme to calculate the temperature field by taking the internal boundary for temperature into consideration. Sato and Ničeno [28] employ a finite difference scheme for the discretization of the temperature by setting T_{sat} at the interface as the boundary condition. Moreover, as an effective approach, GFM is again used to impose the saturated temperature at the interface [32,22]. However, Esmaeeli and Tryggvason [26,27] show that by adding a heat source term representing the latent heat in the energy equation in vicinity of the mixed cells, the calculation of the temperature field is also correct without imposing a boundary condition for it.

Based on the VOF framework, the present study uses a smooth approach to smear the point mass source to the ambient cells close to the interface, for purpose of preserving the numerical stability. Besides, we will show that by controlling the smearing thickness of δ, the scheme is accurate and robust. On the other hand by using a ghost-cell approach, the saturating temperature is imposed as a internal boundary condition at the liquid–vapor interface during solving the energy equation. At the opposite, we provide numerical evidence that without imposing such an accurate boundary condition for the temperature field, it fails to determine accurately the interface advancing or retreating, and thereby, the whole computations are not reliable.

In addition, as the volume averaged scheme on basis of the VOF method smears the discontinuity of the physical properties across the interface, especially when the electric conductivities vary very much between the two phases, the corresponding errors in solving the electromagnetic field need to be further investigated. Based on the Cartesian grids, a series of sharp interface methods have been proposed to enforce the sharp jump conditions on the boundary during solving the Poisson type equations, among which the most known ones are the ghost-fluid methods and embedded boundary methods (EBM, hereafter) [33,34], which is also used in the phase change flows for tackling such discontinuous problem. Recently in simulating the electrohydrodynamics multiphase flows, some researchers [35,36] have also employed the GFM to keep

the discontinuity in the normal component of the electric field, and the results seem to be more promising against the volume-averaged method. However, as far as the authors know, there is no similar method applied for simulating the MHD flows. Therefore, the present study extend the cut-cell method as a kind of EBM to solve the electric potential within the framework of VOF. To take the advantage of Gerris, the interface is reconstructed by sharp piecewise linear segments, and the normal vectors of the interface are also calculated in a sharp manner. After that, a consistent and conservative scheme is applied to compute the current density in the interfacial cells, and by this, the conservative property of the current density could be preserved.

To the best of the authors' knowledge, the present work is the first attempt to develop a numerical method for the direct numerical simulations of incompressible multiphase magnetohydrodynamics with phase change. We mainly focus on the numerical simulations of the MHD influence on the vapor bubble growth in a superheated liquid as well as on the film boiling of the liquid metal. Therefore, after providing numerical evidences that the mass transfer rate and the temperature field can be calculated accurately even with strong density ratio and strong capillary effects, we proceed to simulate the vapor bubble growth in a superheated liquid under gravity and MHD effect, it is an actually challenging issue since the thermal boundary layer around the bubble is very thin in comparison to the bubble diameter, and hence both the accuracy and the stability are important in simulating the rising of such a vaporing and deforming bubble. After that, the simulation of the 3D film boiling flows are further carried out, the magnetic fields are observed to impose great influence on the vapor bubble growth and detachment.

The present paper is organized as follows. In Sec. 2 the complete multiphase MHD equations are presented, particularly for the jump conditions across the interface for the problems being considered in the present study. The application of the cut-cell method in computing multiphase MHD flows is described in Sec. 3, including the numerical algorithms and the numerical tests designed for it. In Sec. 4, the phase change model is proposed and validated by comparing the results with available analytical solutions and experimental data. Besides, by embedding the phase change model into the multiphase MHD solver, the influence of the external magnetic field on the vapor bubble growth in superheated liquid and on the film boiling flows are investigated. At last, the conclusion of the present study and the perspective of the following work are presented in Sec. 5.

2. Governing equations

Consider a general case of multi-phase flow in a domain Ω and a lower dimensional interface Γ that divides Ω into separated phases as Ω_1 and Ω_2. Inside each phase, the governing equations describe the behavior of the fluid flow take the same form as the incompressible Navier–Stokes equations, with the electromagnetic equations being coupled. If there is liquid–vapor phase change happening, we can expect the divergence-free condition of the velocity is no longer valid at the interface, and in addition, an enthalpy conservation equation should be coupled. Moreover, if the liquid–vapor interface Γ is assumed to be electrically insulating, no current density would pass through it that a sharp scheme should be used to calculate the electromagnetic field in the liquid phase.

2.1. The incompressible Navier–Stokes equations

As presented in our previous study [3], the basic equations for viscous incompressible MHD flows that describe the conservation of momentum and mass read

$$\rho(\frac{\partial \boldsymbol{u}}{\partial t} + \boldsymbol{u} \cdot \nabla \boldsymbol{u}) = -\nabla p + \nabla \cdot (\mu(\nabla \boldsymbol{u} + \nabla \boldsymbol{u}^T)) + \boldsymbol{F}_s + \boldsymbol{F}_l + \boldsymbol{S} \tag{1}$$

$$\nabla \cdot \boldsymbol{u} = 0 \tag{2}$$

with density ρ, pressure p and dynamics viscosity μ. $\boldsymbol{F}_s$ stands for the surface tension which only acts at the interface and is formulated as a volume force based on the continuous surface tension force (CSF, hereafter) model. With a constant surface tension coefficient, it has a formulation of

$$\boldsymbol{F}_s = \sigma \kappa \delta_s \boldsymbol{n} \tag{3}$$

where σ is the surface tension coefficient, κ the interface curvature and $\boldsymbol{n}$ the normal vector of interface, the force confined on interface is represented by Dirac distribution function δ_s. In addition, $\boldsymbol{F}_l$ is the volume Lorentz force arising from the electromagnetic induction and it takes the form of

$$\boldsymbol{F}_l = \boldsymbol{J} \times \boldsymbol{B} \tag{4}$$

where $\boldsymbol{J}$ is the induced current density, $\boldsymbol{B}$ is the applied magnetic field. To obtain $\boldsymbol{J}$, we solve the Ohm's law in form of

$$\boldsymbol{J} = \sigma_e(\boldsymbol{E} + \boldsymbol{u} \times \boldsymbol{B}) \tag{5}$$

where $\boldsymbol{E}$ is the induced electric field. When the induced magnetic intensity is much smaller than the external field, for which the magnetic Reynolds number ($R_m = \mu_m \sigma_e L u_0$ where μ_m is termed magnetic permeability) is very small, this equation can be written as

$$J = \sigma_e(-\nabla\varphi + u \times B) \tag{6}$$

where φ is the induced electric potential. According to the charge conservation law, we must enhance

$$\nabla \cdot J = 0 \tag{7}$$

and a combined equation is derived from Eq. (6) and Eq. (7) given by

$$\nabla \cdot (\sigma_e \nabla\varphi) = \nabla \cdot (\sigma_e u \times B) \tag{8}$$

which is the so called electric potential Poisson (EPP, hereafter) equation. Part of the work in the present study is to solve this equation more accurately if the electrical conductivities between the two phases vary too much.

The last term of Eq. (1) includes all the remaining source terms contributed to the fluid flow such as the gravity.

Neglecting the kinetic energy, viscous dissipation and bulk compressibility effect, the enthalpy conservation equation is written as:

$$\frac{\partial T}{\partial t} + u \cdot \nabla T = \nabla \cdot \left(\frac{\lambda}{\rho c_p} \nabla T \right) + \frac{J^2}{\sigma_e \rho c_p} \tag{9}$$

where c_p is the volumetric heat capacity, λ the thermal conductivity and T the temperature. In addition, it is always valid to drop $\frac{J^2}{\sigma_e \rho c_p}$ because of the relatively small value compared to other terms.

2.2. The jump conditions when phase change happens

When the liquid–vapor phase change happens at the interface, there is mass flux $\dot{m}$ produced at the interface and the mass conservation law gives the relation between $\dot{m}$, fluid velocity and the interface velocity as

$$\rho_{liq}(u_\Gamma - u_{liq}) \cdot n = \rho_{vap}(u_\Gamma - u_{vap}) \cdot n = \dot{m} \tag{10}$$

where the subscript liq and vap are the values in the liquid region and the vapor region, respectively. As a consequence, the jump condition of the normal component of the velocity across the interface has a formulation of

$$[\![u]\!] = (\frac{1}{\rho_{vap}} - \frac{1}{\rho_{liq}})\dot{m} \tag{11}$$

where $[\![\,]\!]$ is the normal jump for a given variable across the interface. In addition, the velocity component tangent to the interface is continuous and it has a relationship of

$$u_{liq} \cdot t = u_{vap} \cdot t = u_\Gamma \cdot t \tag{12}$$

where t is the interface tangent vector.

Moreover, by revisiting Eq. (2) when the phase change takes place, the integral form of the continuity equation for a mixed cell should be modified as

$$\oint_\Omega u \cdot n dS = \int_\Gamma (u_{vap} - u_{liq}) \cdot n dS \tag{13}$$

By substituting Eq. (11) into Eq. (13), the continuity equation becomes

$$\oint_\Omega u \cdot n dS = \int_\Gamma (\frac{1}{\rho_{vap}} - \frac{1}{\rho_{liq}})\dot{m} dS \tag{14}$$

Then the differential form is derived as

$$\nabla \cdot u = (\frac{1}{\rho_{vap}} - \frac{1}{\rho_{liq}})\ddot{m} \tag{15}$$

where $\ddot{m}$ is the volume mass transfer rate given by

$$V\ddot{m} = \dot{m} S_\Gamma \tag{16}$$

where V is the volume of the mixed cell, and S_Γ is the length (area for three dimension) of the interface. Correspondingly, $\ddot{m}$ is more like a volume source centered on the interface.

For Eq. (15), the mass transfer rate $\ddot{m}$ or $\dot{m}$ is crucial for the subsequent calculations, and thus it is the first step to give an accurate estimation of it. Actually, the mass flux rate is coming from the energy jump condition of

$$\dot{m} h_{lg} = [\![\boldsymbol{q}]\!] \tag{17}$$

$$\dot{m} = \frac{(\boldsymbol{q}_{liq} - \boldsymbol{q}_{vap}) \cdot \boldsymbol{n}}{h_{lg}} = \frac{\left((\lambda \nabla T)_{liq} - (\lambda \nabla T)_{vap} \right) \cdot \boldsymbol{n}}{h_{lg}} \tag{18}$$

where h_{lg} is the latent heat. As aforementioned in Sec. 1, the interface is assumed to keep at the saturating temperature during the phase change, therefore we enhance

$$T_\Gamma = T_{sat}(p_\infty) \tag{19}$$

where p_∞ is the saturating pressure.

This assumption is adequate for most problems, however for particular flows with very high heat fluxes across the interface, a more complete expression for the interface temperature has been presented by Juric and Tryggvason [37], and it has also been used by Hardt and Wondra [17]. Nevertheless, to be more specific, the liquid metal used in the MHD flows always suffers from the oxidations that the behaviors of the metallic interface are changed, and hence the heat transfer across the liquid–vapor interface would be different, such influences should be estimated to model the heated surface as a boundary condition. In addition, the critical heat flux boiling (CHF) conditions are also very important in designing and maintaining the safety of fusion reactor that they also deserve more knowledge. However, for the test cases presented in this study, such complicated situations are not considered at present.

Besides the velocity jump condition of Eq. (11) and the thermal flux jump condition of Eq. (17), the surface tension force, the Lorentz force, the normal tangential stress jump and mass flux all contribute to the jump in the pressure, given as

$$[\![p]\!] = \sigma \kappa + (\tau_{liq} - \tau_{vap}) \cdot \boldsymbol{n} + (\boldsymbol{F}_{l(liq)} - \boldsymbol{F}_{l(vap)}) \cdot \boldsymbol{n} - (\boldsymbol{u}_{vap} - \boldsymbol{u}_{liq}) \cdot \boldsymbol{n} \dot{m} \tag{20}$$

where τ is the normal viscous stress. It should be kept in mind that the dependency of σ on the temperature field is not considered in the present study.

2.3. The jump conditions across the electrically insulating interface

It is frequently encountered in the fusion and metallurgic engineering that an electrically conducting (insulating) fluid moving in the ambient insulating (conducting) fluid, in such case, the electrically insulating interface Γ can be viewed as a barrier to lock the electric field inside the electrically conducting phase, namely Ω_1. In other words, the normal component of the current density should be zero at the interface, given as

$$\boldsymbol{J} \cdot \boldsymbol{n} = 0 \tag{21}$$

Alternatively, it is more like to provide an internal boundary condition for the EPP equation of Eq. (8), that is

$$\nabla \varphi \cdot \boldsymbol{n} = (\boldsymbol{u}_\Gamma \times \boldsymbol{B}) \cdot \boldsymbol{n} \tag{22}$$

Eq. (22) actually gives an inhomogeneous Neumann boundary condition for the electric potential during the translating and deforming of the interface Γ. Moreover, the electric potential and the current density are both continuous across the interface, indicating that

$$[\![\boldsymbol{J}]\!] = 0 \tag{23}$$

$$[\![\varphi]\!] = 0 \tag{24}$$

However, the flux of the gradient of electric potential across the interface is not continuous, and the jump condition is given as

$$[\![\sigma_e(\nabla \varphi)]\!] = [\![\sigma_e(\boldsymbol{u} \times \boldsymbol{B})]\!] \tag{25}$$

Eq. (25) is simplified to $[\![\sigma_e(\nabla \varphi)]\!] = [\![\sigma_e]\!](\boldsymbol{u} \times \boldsymbol{B})_\Gamma$ when both $\boldsymbol{u}$ and $\boldsymbol{B}$ are continuous across the interface without considering the phase change to happen at the interface. By this equation, in addition, we would find that if the interface is an insulated solid boundary, giving $\boldsymbol{u} = \boldsymbol{0}$, the jump condition would be $[\![\sigma_e(\nabla \varphi)]\!] = \boldsymbol{0}$ and this is just a particular case in the present study.

With reference to the electromagnetic field tangent to the interface, it is always continuous as similar as that in Eq. (12).

3. Cut-cell method for mixed cells

Before proposing the MHD phase change model, a cut-cell method is firstly introduced to compute the electromagnetic field in the multi-phase MHD flows in order to preserve the sharpness of the computation of the electromagnetic field inside the conducting phase. Furthermore, some test cases are further carried out to validate the accuracy and the superiority of the method in solving the EPP equation and the current density.

(a) volume averaged scheme   (b) cut-cell scheme
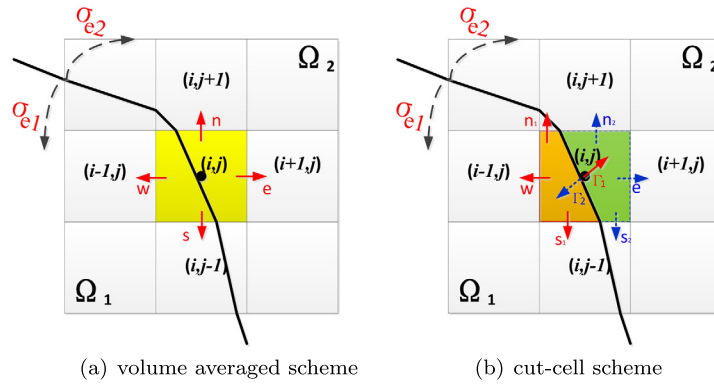
Fig. 1. The integrate form of the fluxes on the boundaries of the mixed cell, respectively with (a) the volume averaged scheme and (b) the cut-cell scheme.

3.1. Numerical methods

As mentioned earlier, the VOF method is employed to track and advance the interface, and the conservative form of the equation is given as

$$\frac{\partial f}{\partial t} + \nabla \cdot (\boldsymbol{u} f) = 0 \tag{26}$$

where f is the volume fraction of the liquid (gas or vapor) phase in the cell.

The Eulerian-implicit–explicit scheme, as described by Rider and Kothe [38], is used for the volume fraction advection that f is updated in split directions, respectively. In addition, in order to avoid numerical diffusion of the interface, the volume fluxes across the cell faces are estimated using the piecewise geometry of the reconstructed interface [39], and the scheme is simply implemented in the Cartesian grids. The discretization form of Eq. (26) is

$$\frac{f^{n+\frac{1}{2}} - f^{n-\frac{1}{2}}}{\Delta t} + \nabla \cdot (f^n \boldsymbol{u}^n) = 0 \tag{27}$$

where the superscript n is the time step. More details about how to conserve the consistency of the volume flux on the coarse-fine cell faces are described by Popinet [4], and they will not be repeated here.

After updating $f^{n+1/2}$, the physical properties of the fluid density and viscosity are calculated with a volume averaged method, given as $\phi = \phi_1 f + \phi_2 (1 - f)$, where the subscript 1 and 2 are the liquid and gas (vapor) phase, respectively. It is a continuous method which smears the discontinuity of ρ and μ across the interface, however such a treatment is widely adopted within the VOF framework because of its simplicity and robustness. Although some researchers try to preserve the discontinuous property of the viscous stress across the interface by applying the GFM [40], however, the improvement is not so evident.

In our previous study [3], this volume averaging scheme is also used to estimate the electric conductivity in the mixed cells, however, different from the calculation of ρ or μ, it is widely known [5,41] that to keep the conservative property of the current density inside the conducting phase has great significance in simulating the MHD flows, that is to say, the current density should not pass through the electrically insulating interface that the sharpness of the interface needs to be preserved. For instance, for a given Poisson equation in form of

$$\nabla \cdot (\sigma_e \nabla \varphi) = \sigma_e \theta \tag{28}$$

The integral form is

$$\sum_{f=1}^{nf} (\sigma_e \nabla \varphi)_f \cdot \boldsymbol{n}_f S_f = \sigma_e \theta V \tag{29}$$

where the subscript f denotes the cell face, S_f the area of the cell face and V the cell volume. θ is the right-hand side of the Poisson equation, $\boldsymbol{n}_f$ is the normal direction of the cell face and nf is the number of total cell faces of the cell. If the cell is entirely located in Ω_1 or Ω_2, then no particular attention should be paid during discretization of the equation. However, if the cell is cut by Γ that the coefficient σ_e is not continuous any more, extra attention should be paid. The volume averaged scheme for a mixed cell (i, j) is schematically illustrated in Fig. 1(a), and we will not present the discretized scheme here since it is widely accepted.
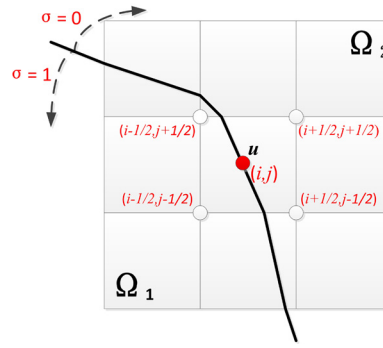
Fig. 2. The interpolation schemes for $\boldsymbol{u}$ in the mixed cells, after $\boldsymbol{u}$ is determined at the centroid position of the interface, then $(\frac{\partial \varphi}{\partial n})^\Gamma = (\boldsymbol{u} \times \boldsymbol{B})^\Gamma \cdot \boldsymbol{n}$ can be used to estimate the flux across the interface.

In contrast, within the cut-cell approach, which is always used for treating the complex solid boundaries, the partial fractions of cell (i, j) containing in Ω_1 and Ω_2 are handled separately, as drawn in Fig. 1(b). From the figure, the discretization of Eq. (29) in Ω_1 contained in cell (i, j) is written as

$$(\sigma_e \frac{\partial \varphi}{\partial n})^e S^e f^e - (\sigma_e \frac{\partial \varphi}{\partial n})^w S^w f^w + (\sigma_e \frac{\partial \varphi}{\partial n})^n S^n f^n - (\sigma_e \frac{\partial \varphi}{\partial n})^s S^s f^s + (\sigma_{e1} \frac{\partial \varphi}{\partial n})_1^\Gamma S^\Gamma = \sigma_{e1} \theta V f \tag{30}$$

where $f^e \sim f^s$ is the area fraction of corresponding face lying inside Ω_1. In the cut-cell approach, $(\sigma_e)^e \sim (\sigma_e)^s$ is no longer the averaged value on the cell face but it is just σ_{e1} as a sharp estimation. In Fig. 1(b), the integration on the east face is eliminated because $f^e = 0$. Therefore, Eq. (30) finally takes the form of

$$-(\sigma_{e1})(\frac{\partial \varphi}{\partial n})^w + (\sigma_{e1} f^n)(\frac{\partial \varphi}{\partial n})^n - (\sigma_{e1} f^s)(\frac{\partial \varphi}{\partial n})^s + (\sigma_{e1} \frac{\partial \varphi}{\partial n})_1^\Gamma S^\Gamma = (\sigma_{e1} f)\theta \tag{31}$$

In the same method, the discretization of Eq. (29) in Ω_2 contained in cell (i, j) is derived as

$$(\sigma_{e2})(\frac{\partial \varphi}{\partial n})^e + (\sigma_{e2}(1 - f^n))(\frac{\partial \varphi}{\partial n})^n - (\sigma_{e2}(1 - f^s))(\frac{\partial \varphi}{\partial n})^s - (\sigma_{e2} \frac{\partial \varphi}{\partial n})_2^\Gamma S^\Gamma = (\sigma_{e2}(1 - f))\theta \tag{32}$$

In addition, if Ω_2 is assumed to be electrically insulating, then Eq. (32) is vanished that only Eq. (31) is retained. Then the key points are how to estimate $f^e \sim f^s$, $(\frac{\partial \varphi}{\partial n})^e \sim (\frac{\partial \varphi}{\partial n})^s$ and $(\frac{\partial \varphi}{\partial n})^\Gamma$ in the mixed cells, respectively.

In summary, to solve the discretized form of Eq. (31) within the cut-cell approach, the key issues and our solutions are as follows

- **The estimation of $(\frac{\partial \varphi}{\partial n})^f$ at the partial face of the mixed cells.** Relevant to using of EBM for treating the complex solid boundaries on the Cartesian grids, it is suggested to use an interpolation scheme to calculate $(\frac{\partial \varphi}{\partial n})$ at the midpoint of the partial face from the adjacent full faces [42–44], and the scheme preserves the second-order accuracy. However, in Gerris when treating the solid boundary with the EBM, the full-face-centered gradient is still used in the mixed cells because it is difficult to adapt the partial-face-centered scheme to the AMR framework. To be consistent with the interpolation schemes constructed in Gerris, we also use the full-face-centered gradient operator when the cell faces are cut by the interface Γ. Moreover, we will show later that even using such an gradient operator, the convergence rate of the solutions still keeps at second-order.

- **The estimation of $(\frac{\partial \varphi}{\partial n})^\Gamma$ at the fluid–fluid interface.** For an electrically insulated solid boundary, this is a very easy problem because the no-slip boundary condition leads to a homogeneous Neumann boundary condition of $(\frac{\partial \varphi}{\partial n})^\Gamma = 0$. However, as the interface translates and deforms with the fluid, the boundary condition at the electrically insulated interface would be $(\frac{\partial \varphi}{\partial n})^\Gamma = (\boldsymbol{u} \times \boldsymbol{B})^\Gamma \cdot \boldsymbol{n}$, as shown in Eq. (22). Because the velocity field and the magnetic field are continuous across the interface when no phase change happens, an interpolation scheme from the surrounding cells is used to estimate $\boldsymbol{u}$ and $\boldsymbol{B}$ at the centroid position of the interface. As shown in Fig. 2, the value of $\boldsymbol{u}$ at the midpoint of the interface is interpolated from the velocities at cell vertexes which are further averaged from the surrounding four (eight for three dimension) cells. Furthermore, even when the phase change is taken into consideration, the interface velocity can still be calculated from Eq. (11) by applying the jump condition. In addition, the normal vectors of $\boldsymbol{n}$ are calculated by the reconstructed piecewise linear segments, so it is not a diffusive but a sharp scheme.

- **The estimation of the flux on the partial coarse-fine faces.** As mentioned earlier, the fluid–fluid interface is reconstructed by a series of piecewise linear segments, and therefore the calculations of the partial area of the cell faces use a sharp scheme. However, the emphasis is how to preserve the consistency of the estimation of flux at the coarse-fine cell boundaries. As shown in Fig. 3, "flux1" is the flux of $(\frac{\partial \varphi}{\partial n})S_1 f_1$ at the west face of cell $(i + 1, j)^+$ and "flux2" is the flux of $(\frac{\partial \varphi}{\partial n})S_2 f_2$ at the west face of cell $(i + 1, j)^-$, under such circumstance, the flux at the east face of cell (i, j) is
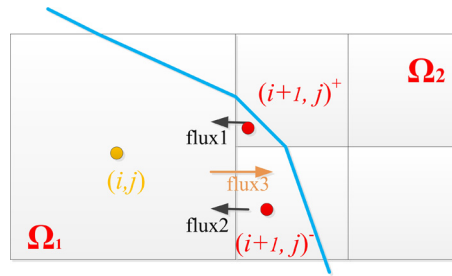
Fig. 3. A consistent estimation of the flux on the partial coarse-fine faces of the mixed cell.

calculated as flux3 $= \frac{\partial \varphi}{\partial n} S_1 f1 + \frac{\partial \varphi}{\partial n} S_2 f2$ to make the flux estimation be consistent. More detailed description of this part can be found in the work of S. Popinet [45], and we will not repeat it here.

To implement the cut-cell approach in the available multi-phase MHD solver, a new structure is defined with the name of *GfsVOFstate*, which contains the following information for the cell: (1) the volume fraction f of the conductive liquid phase; (2) the face fraction $s[f]$ of the conductive liquid phase on each face; (3) the length l (area for 3D) and the centroid position of the interface in the mixed cells. In addition, we also discriminate different cell states from "perfectly conducting cells", "mixed cells" and "perfectly insulating cells" according to the value of the volume fraction f.

After obtaining the electric potential by applying the proposed cut-cell approach, then a conservative formula for Lorentz force calculation is given as follows [41]

$$\boldsymbol{F}_l = \boldsymbol{J} \times \boldsymbol{B} = \nabla \cdot (\boldsymbol{J}(\boldsymbol{r} \times \boldsymbol{B})) = \nabla \cdot (\boldsymbol{J}\boldsymbol{r}) \times \boldsymbol{B} \tag{33}$$

where $\boldsymbol{r}$ is the distance vector. It indicates that the current density also has a conservative form of

$$\boldsymbol{J} = \nabla \cdot (\boldsymbol{J}\boldsymbol{r}) \tag{34}$$

In our previous studies [3,6] for the single phase flows with complex solid boundaries, this scheme is proved to be important in obtaining a more accurate solution of the current density compared with the ordinary "fraction averaged" scheme, which is as follows

$$(J_x)_c = \frac{J_x^e f^e + J_x^w f^w}{f^e + f^w}, \quad (J_y)_c = \frac{J_y^n f^n + J_y^s f^s}{f^n + f^s}. \tag{35}$$

Actually, Eq. (34) and Eq. (35) are equal when the cell is fully rectangular, as validated by Ni et al. [41]. However, Eq. (35) will cause error in computing the current density in presence of strong magnetic field since it can not keep the conservative property of the Lorentz force. By using the conservative scheme, the current density at the cell center is calculated as [41, 46,6]

$$\begin{aligned}
\boldsymbol{J}_c &= \frac{1}{V} \int_V \boldsymbol{J} dV = \frac{1}{V} \int_V \nabla \cdot (\boldsymbol{J}(\boldsymbol{r} - \boldsymbol{r}_c)) dV \\
&= \frac{1}{V} \oint_V (J_n(\boldsymbol{r} - \boldsymbol{r}_c)) dS \\
&= \frac{1}{V} \sum_{f=1}^{nf} (J_n)_f (\boldsymbol{r}_f - \boldsymbol{r}_c) S_f \\
&= \frac{1}{V} \sum_{f=1}^{nf} (J_n)_f S_f d_f \boldsymbol{n}_f
\end{aligned} \tag{36}$$

herein, we use an expression of $\boldsymbol{r}_f - \boldsymbol{r}_c = d_f \boldsymbol{n}_f$, where d_f denotes the distance from cell center to face center.

Different from our previous study [3] which uses the faction averaged scheme of Eq. (35) to interpolate the current density, Eq. (34) and Eq. (36) are employed in the present study. With this conservative interpolation operator, the Lorenz force $\boldsymbol{J}_c \times \boldsymbol{B}_c$ is further computed in mixed cells.

3.2. Numerical tests

In this part, some numerical tests are presented to validate the accuracy of the cut-cell scheme used in solving the EPP equation and the application of the conservative scheme for the calculation of Lorentz force is also verified. In the tests, not only the static interface, but also the translated and deformed interface is under consideration.
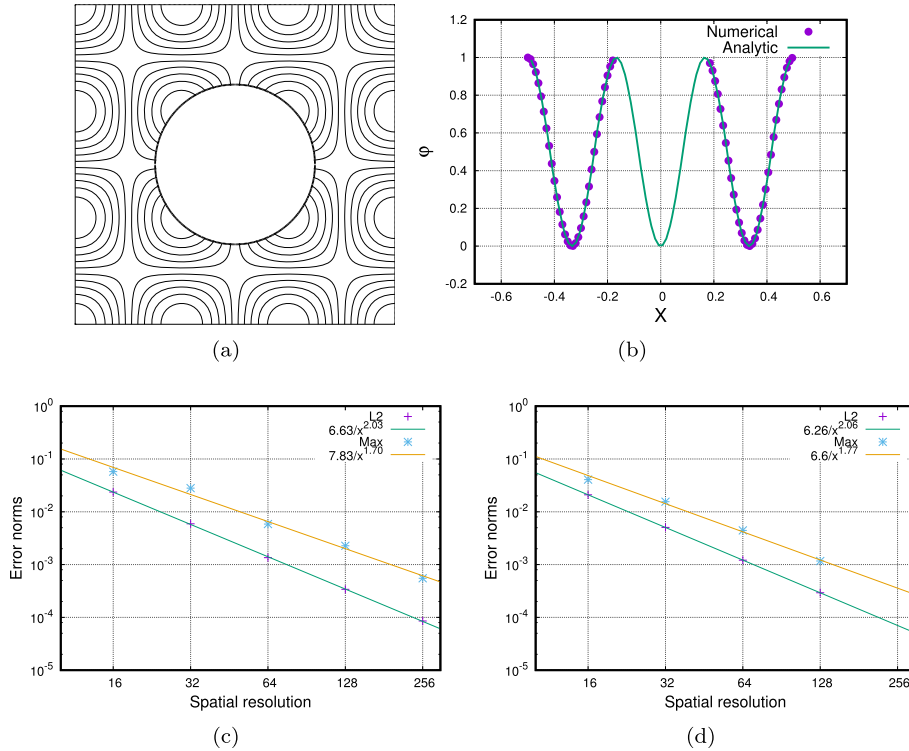
Fig. 4. The solution of Poisson problems by using the cut-cell method to treat the interface, the Neumann boundary condition is applied at the interface. From left to right, top to bottom: (a) The contour map of φ in the domain of Ω_1; (b) The distribution of φ along the diagonal line from left bottom to the right top of the domain, and the analytical solutions are plotted as comparisons; (c) The evolution of the error and associated convergence order on the uniform grids; (d) The evolution of the error and associated convergence order on the adaptive grids.

3.2.1. With a static interface

The test case we present here is also given by Popinet [45], and the right-hand side of Eq. (28) is

$$\theta = -\pi^2 (k^2 + l^2) sin(\pi kx) sin(\pi ly) \tag{37}$$

with $k = l = 3$. By assuming the coefficient to be $\sigma_e = 1$, the exact solution of the Poisson equation is

$$\varphi(x, y) = sin(\pi kx) sin(\pi ly) \tag{38}$$

The computational domain is a unit square, and the interphase Γ separates the domain into two parts: Ω_1 outside and Ω_2 inside. As a simple geometry, a circular interface $\Gamma = \{\Omega_1 : x^2 + y^2 - (\frac{1}{4})^2 > 0\}$ is firstly introduced to verify the validity of the numerical scheme. With the cut-cell approach, the boundary condition imposed on the interface is derived from the analytical solution of Eq. (38), given as: (1) $\frac{\partial \varphi}{\partial n} = (\frac{\partial \varphi}{\partial x}, \frac{\partial \varphi}{\partial y}) \cdot (n_x, n_y)$ for the Neumann condition, and (2) $\varphi = \varphi(x_0, y_0)$ for the Dirichlet condition, where the coordinate (x_0, y_0) is the centroid position of the interface. In this test, the local normal vectors of the interface is calculated as $(n_x, n_y) = (\frac{x}{R}, \frac{y}{R})$ where R is the radius of the circle. The coefficient of σ_e is set as $\sigma_e = 1$ in Ω_1 and $\sigma_e = 0$ in Ω_2 respectively. The computational domain is discretized using uniform grids, with levels of 4, 5, 6, 7, 8 by setting 16, 32, 64, 128, 256 meshes along the width of the domain, respectively.

With the Neumann boundary condition, the contour plots of φ in Ω_1 is plotted in Fig. 4(a). The distribution of φ along the diagonal line from the left bottom to the right top of the domain is presented in Fig. 4(b), whereas the numerical results are observed to fit very well with the analytical solution. Moreover, the norms of the error as a function of spatial resolution is illustrated on Fig. 4(c), and a second-order accuracy is obtained irrespectively for the root-mean-square norm of error or the maximum error. It is not surprise that Popinet [45] also obtains the second-order convergence by using the similar cut-cell approach even if the calculation of $(\frac{\partial \varphi}{\partial n})^f$ on partial cell face is only first-order accurate near the solid boundaries. In addition, if the AMR technique is applied to save the computational resources that two more levels are refined near the interface, the error norms are presented in Fig. 4(d), whereas a second-order accuracy is still observed.

Through the above tests, it is validated that the proposed cut-cell approach is accurate in solving the Poisson problems with a Neumann boundary condition, and even with the AMR technique, the second-order accuracy is preserved.
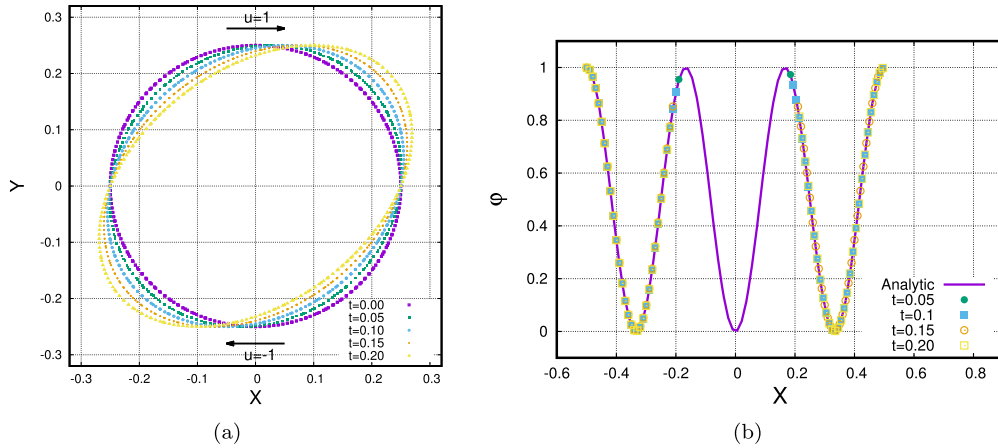
Fig. 5. The solution of Poisson problems by using the cut-cell method to treat the translated and deformed interface. (a) The evolution of the interface shape over time; (b) The distribution of φ along the diagonal line from left bottom to the right top of the domain, and the analytical solutions are plotted for comparisons.

3.2.2. A translating and deforming interface

In this test case, the accuracy of the cut-cell method is further investigated when the interface is translating and deforming with the flow. We still use the circular interface of $\Gamma = \{\Omega_1 : x^2 + y^2 - (\frac{1}{4})^2 > 0\}$ as the initial shape. However, the interface keeps moving and rotating in the shear flow. For this purpose, we solve the same Poisson equation as above, but constant horizontal velocities are imposed at the top and bottom boundary of the domain, given as $u = 1$ and $u = -1$ respectively. The evolution of the interface shape in Fig. 5(a) shows that as the time lapses, the initially circular interface rotates and elongates in the shear flow. In Fig. 5(b), the distributions of φ along the diagonal line are also plotted at different time instants, it is observed that the numerical results are always in good agreement with the analytical solutions all the time.

Through this test case, it is validated that even though the interface translates or deforms with the flow, the cut-cell approach based on the time-dependent reconstructing scheme for the interface is always robust and accurate.

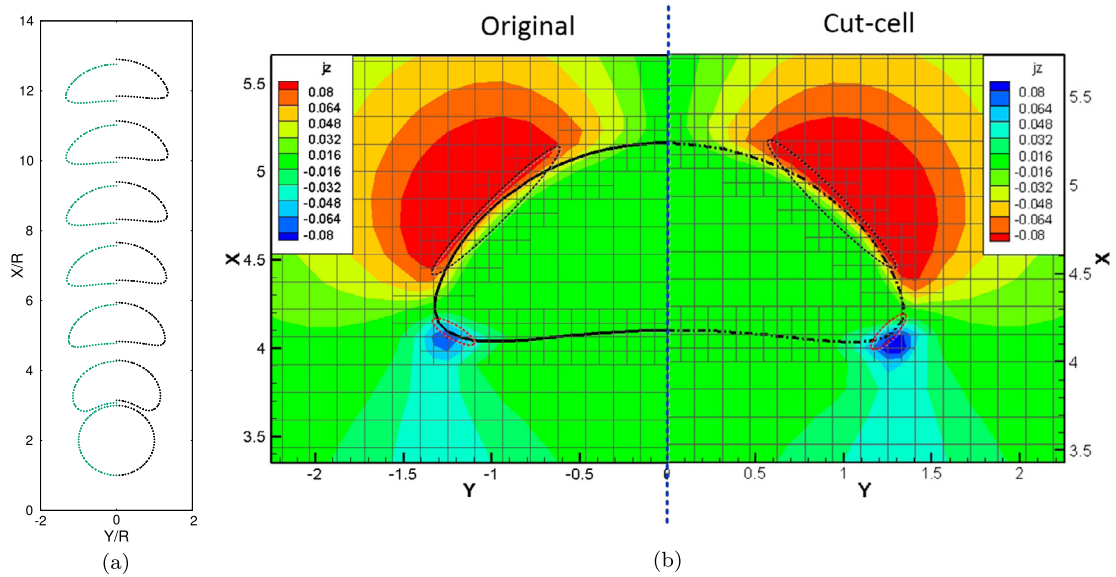### 3.2.3. Three-dimensional bubble rising in MHD flows

The rise of a three-dimensional air bubble in presence of vertical magnetic field is further simulated by using the original algorithms and the cut-cell approach coupled with the conservative formula for Lorentz force calculation. The characteristic non-dimensional number of this situation is the Bond number of $Bo = \rho g R^2 / \sigma$ and the Galilei number of $Ga = \rho \sqrt{gR} R / \mu$, where R is the initial radius of the bubble. When external magnetic field is imposed, the interaction number is used to weigh the influence of Lorentz force over gravity, being $N = \sigma_e B^2 R / (\rho \sqrt{gR})$ in the present study. The computational domain is chosen as $20R \times 10R \times 10R$ and the bubble of $R = 1$ is set at $(3R, 0, 0)$, with the gravity to direct along x-axis.

The contrasts of the physical properties between the fluid and air are respectively of $\rho_{liq}/\rho_{air} = 1000$, $\mu_{liq}/\mu_{air} = 100$ and $\sigma_{e(liq)}/\sigma_{e(air)} = 10^5$, while other non-dimensional parameters are $Bo = 10$, $Ga = 10$ and $N = 0.3$, respectively. The time histories of bubble shapes in the vertical center plane are shown in Fig. 6(a) at different non-dimensional times, respectively of $t = 0, 2, 4, 6, 8, 10$ and 12. It should be noted that the left half of the figure is the result by using the original VOF method, while the right half uses the cut-cell approach coupled with the conservative formula for Lorentz force calculation. It is observed that slight differences are observed at the rising height of the bubble between the two methods.

To give closer analysis on this issue, the contour map of the z-component current density in vicinity of the bubble interface is presented in the vertical center plane $((x - y)$ plane), as shown in Fig. 6(b) for non-dimensional time of $t = 9$. In the figure, the left half still represents the original VOF method while the right half uses the improved algorithms. In addition, it should be noted that for the convenience of comparison, the contour levels in the right half is reversed. As shown in the dashed ellipse inside the figure, it is observed that the diffusion layer of J_z in the air side is thinner by using the improved numerical method, indicating that the sharpness of the computing of the electromagnetic field is better preserved. With such improvement, the computations of the Lorentz force are also different, and hence the computed bubble rising behavior are not identical between them.

4. The phase change model

In this section, a phase change model is proposed on basis of the multiphase MHD solver. The validity of the numerical scheme is verified by comparing the results with some available analytical and experimental solutions. At last, the three dimensional vapor bubble rising in superheated liquid and the film boiling flows under the influence of external magnetic fields are further investigated.

Fig. 6. Three-dimensional bubble rises in MHD flows, with non-dimensional parameters of $Bo = 10$, $Ga = 10$ and $N = 0.3$, respectively. (a) The bubble shapes and rising heights by using the original VOF method (left) and the improved algorithms (right); (b) contour maps of J_z in vicinity of the bubble interface at the vertical center $(x - y)$ plane, respectively computed by the original VOF method (left) and the improved algorithms (right). (For interpretation of the colors in the figure(s), the reader is referred to the web version of this article.)
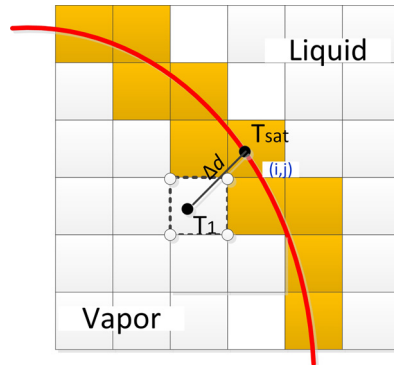
Fig. 7. The numerical scheme for estimating $\frac{\partial T}{\partial n}$ at the interface from the vapor phase.

4.1. Numerical methods

As shown in Sec. 2, the first step to construct the phase change model is to calculate the heat flux at the liquid–vapor interface, giving by Eq. (18). From the equation, the key issue in estimating $\llbracket q \rrbracket$ is to calculate $\frac{\partial T}{\partial n}$ at the interface from the liquid side and the vapor side, respectively. For sake of brevity, only the discretization of $\left(\lambda \left(\frac{\partial T}{\partial n} \right) \right)_{vap}$ from the vapor phase will be described below that the discretization in the liquid side can be obtained in an analogous manner. According to Fig. 7, the mixed cell (i, j) is taken as an example to describe the numerical method. As shown in that figure, $\left(\frac{\partial T}{\partial n} \right)_{vap}^{\Gamma}$ at the interface from the vapor side is approximated as

$$\left(\frac{\partial T}{\partial n} \right)_{vap} = \frac{T_1 - T_{sat}}{\Delta d} \tag{39}$$

where T_1 denotes the temperature at the local position by extending the line l running through the centroid point of the interface along the normal vector direction $\boldsymbol{n}$ to a distance of Δd. Herein, both the centroid point and the normal vector of the interface are estimated by the piecewise linear segments, which is sharp without any thickness. The extended distance Δd is not so strictly defined that we find the results are insensitive to its length when $\Delta < \Delta d < 2\Delta$, Δ being the cell size. This is also indicated by Esmaeeli and Tryggvason [26], in addition, our numerical experiments find that by using a three-points gradient interpolator, the accuracy does not show appreciable improvement.

In cell $(i - 1, j - 1)$ where T_1 is estimated, the corner values, namely T_{cor} as shown by the hollow circles, are required to obtain T_1 by averaging. And previously, the corner values T_{cor} are interpolated from the surrounding four cells (eight for
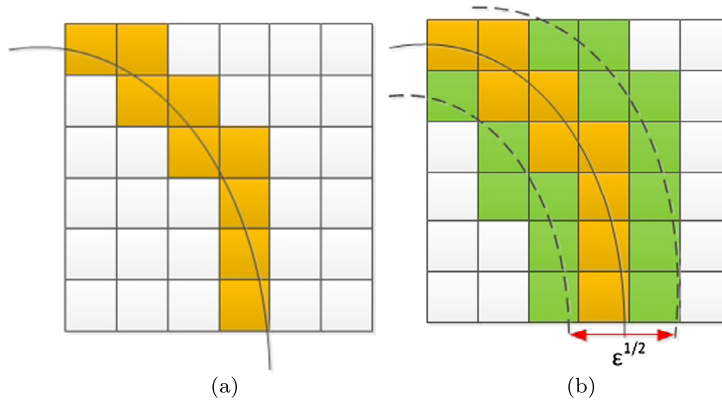
Fig. 8. The cells containing the mass source. (a) Before applying the diffusion equation, $\ddot{m}$ only exists in the mixed cells; (b) after applying the diffusion equation, $\ddot{m}$ is smeared to the neighbor cells with a diffusion thickness, which is scaled as $\sqrt{\varepsilon}$.

three dimension). In particular, when some of the corners are very close to the interface, such as the northeast corner of cell $(i-1, j-1)$, it seems to be problematic in estimating T_{cor} by using the averaged scheme because three of its surrounding cells are cut by the interface. Usually, a more accurate interpolation scheme uses T_{sat} at the interface centroid instead of T at cell center to calculate T_{cor}. However, as we will introduce later, by using a ghost cell method, there is no difference between the two schemes in the present numerical simulations.

When the mixed cell (i, j) is very close to the domain boundary, particular attention should be paid in estimating $\frac{\partial T}{\partial n}$ at the interface, because the cell $(i-1, j-1)$ may lie outside the boundary. In such case, we estimate T_1 at the intersection point between l and the domain boundary, and afterwards, $\frac{\partial T}{\partial n}$ is calculated in the same manner.

After obtaining $\dot{m}$ by using Eq. (18), the volume mass transfer rate of $\ddot{m}$ is calculated by Eq. (16), which can be further applied to solve the continuity equation of Eq. (15). Let us revisit the discretization steps of the approximate projection method used in Gerris [45] and the multi-phase MHD solver [3]. The prediction step is first applied, yielding the prediction velocity at the cell center, given as

$$\rho^{n+\frac{1}{2}}(\frac{\boldsymbol{u}^* - \boldsymbol{u}^n}{\Delta t} + \boldsymbol{u}^{n+\frac{1}{2}} \cdot \nabla \boldsymbol{u}^{n+\frac{1}{2}}) = -\nabla p^n + \nabla \cdot (\mu^{n+\frac{1}{2}}(\boldsymbol{D}^n + \boldsymbol{D}^*)) + (\boldsymbol{J} \times \boldsymbol{B})^n \tag{40}$$

where $\boldsymbol{D}$ is $(\nabla \boldsymbol{u} + \nabla \boldsymbol{u}^T)/2$. After that, a correction step is succeeded as

$$\boldsymbol{u}^{n+1} = \boldsymbol{u}^{**} - \frac{\Delta t}{\rho^{n+\frac{1}{2}}} \nabla(p^{n+1} - p^n) \tag{41}$$

where $\boldsymbol{u}^{**}$ is the predicted velocity after being corrected by the surface tension force at the cell face, and that is given by

$$(\boldsymbol{u}^{**})^f = (\boldsymbol{u}^*)^f + (\frac{\Delta t \sigma \kappa^{n+\frac{1}{2}} \delta_s \boldsymbol{n}}{\rho^{n+\frac{1}{2}}})^f \tag{42}$$

By coupling Eq. (41) with the continuity equation of Eq. (15), the following pressure Poisson equation is obtained

$$\nabla \cdot (\frac{\Delta t}{\rho^{n+\frac{1}{2}}} \nabla(p^{n+1} - p^n)) = \nabla \cdot (\boldsymbol{u}^{**})^f - (\frac{1}{\rho_{vap}} - \frac{1}{\rho_{liq}})\dot{m}\delta_s \tag{43}$$

where δ_s is the Dirac distribution.

However, without δ_s, there probably produces numerical instabilities during solving the pressure Poisson equation because $(\frac{1}{\rho_{vap}} - \frac{1}{\rho_{liq}})\dot{m}$ acts as a point mass source which only exists in the mixed cells. Fig. 8(a) is used for illustration that only the colored cells cut by the interface contain $\ddot{m}$. Besides using the sharp scheme such as GFM to preserve the jump condition for the normal velocity across the interface, some other methods employ smooth functions to distribute the mass source into the neighbor cells. The numerical method used in the present study belongs to the second category that we transfer the mass source into the surrounding cells by solving a diffusion equation, which is proposed by Hardt and Wondra [17]. The diffusion equation is given as

$$\nabla \cdot (\varepsilon \nabla \ddot{m}') = \ddot{m} \tag{44}$$

where ε is used to control the thickness of the diffusion layer, which is scaled as $\sqrt{\varepsilon}$. It is also validated that this model guarantees the mass source to be conserved after smearing them to the surrounding cells. After solving the diffusion equation, the cells containing the mass source are shown in Fig. 8(b).
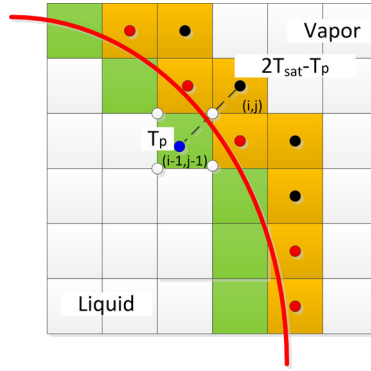
Fig. 9. The calculation of the temperature field in the ghost cells lying outside the liquid phase. This method is used to maintain the interface at the saturated temperature.

After the smearing procedure, the new mass source of $\ddot{m}'$ is substituted into Eq. (43) to solve p^{n+1}. Subsequently, $\mathbf{u}^{n+1}$ is further updated by solving Eq. (41).

The equation for the interface advancing also requires modification because of the mass transfer, given as

$$\frac{\partial f}{\partial t} + \nabla \cdot (\mathbf{u} f) = \frac{\ddot{m}}{\rho_{vap}} \tag{45}$$

and except for the source term due to mass transfer, the other discretization steps in this equation are as the same as in Eq. (27).

At last, the discretization of the temperature field is also presented, and this is already given in our previous study [3] in forms of

$$\frac{T^{n+\frac{1}{2}} - T^{n-\frac{1}{2}}}{\Delta t} + (\mathbf{u} \cdot \nabla T)^{n+\frac{1}{2}} = \nabla \cdot \left(\left(\frac{\lambda}{\rho c_p} \right) \nabla T \right)^{n+\frac{1}{2}} \tag{46}$$

However, unlike the ordinary passive tracer, the temperature field will impose a counteractive effect on the velocity field in the phase change flows, because the jump condition of the velocity across the interface depends on the gradient of the temperature. Therefore, it would be very sensitive in solving the coupling problem between the flow field and the temperature field. Under such circumstance, the most important issue discussed in Sec. 1 is to maintain the liquid–vapor interface at the saturating temperature. In the present study, a ghost cell method is used to impose such a boundary condition on the interface. Herein, only the numerical methods in the liquid phase is introduced that it is an analogous manner to apply the method in the vapor phase.

As shown in Fig. 9, the numerical procedures are as follows:

- First, the ghost cells outside the liquid region need to be identified. They can be classified into two types: (1) the mixed cell whose center is outside the interface, as labeled by the red circle; (2) the pure vapor cell which has a corner neighbor belonging to the mixed cells but not belonging to the ghost cells, as labeled by the black circle.
- Second, the temperature in the ghost cells are calculated. Taking the ghost cell (i, j) as an example, a line l running through the centroid of the cell along the normal vector direction of the interface is extended to the liquid phase, until an mirror point P is found in cell $(i-1, j-1)$. Then $T(i, j) = 2T_{sat} - T_p$ is calculated as the artificial temperature in the ghost cell. As a consequence, the key issue here is to estimate T_p at the mirror point. Again, we still use the interpolation scheme from the cell corners, as shown by the hollow circles. Nevertheless, the problem still exists if the temperature at one of the cell corners needs to be averaged from the ghost cells, as the northeast corner of cell $(i-1, j-1)$. Under such circumstance, not only $T(i, j)$ is depended on T_p, but also T_p is depended on $T(i, j)$. Therefore, an iterative computation is applied to get a convergent solution until the error of $(T^{k+1}(i, j) - T^k(i, j))$ between two adjacent iterative steps is smaller than 10^{-6}. Numerical experiments show that 5 steps are generally enough to get a convergent solution.
- At last, Eq. (46) is solved by setting a group of ghost cells outside the liquid phase.

To sum up, the numerical procedure for one time step is given as follows:

1. The heat flux across the interface is calculated by estimating the temperature gradient at the liquid and vapor sides, respectively. After that, the mass transfer rate is calculated by Eq. (18).
2. A diffusion equation is solved to smear the volume mass source into the neighbor cells, as shown by Eq. (44).
3. The interface position is advanced by solving Eq. (45), and the physical properties are updated by a volume average scheme except the electric conductively.
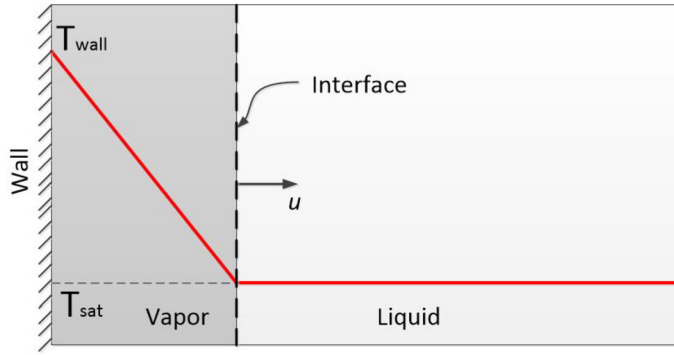
Fig. 10. The schematic diagram of the one dimensional Stefan problem.

4. The temperature equation of Eq. (46) is solved by applying the ghost cell method.
5. The electromagnetic field is computed by solving the EPP equation and the Ohm's law, respectively of Eq. (8) and Eq. (5).
6. Taking the Lorentz force and the mass source into consideration, an approximate projection method is applied to solve the pressure and velocity for the next time step.

4.2. Numerical tests

In the following study, several numerical tests are firstly performed to validate the usability of the proposed model in simulating the phase change flows. After that, the three dimensional vapor bubble rising in a superheated liquid under gravity and the film boiling flows in presence of magnetic fields are computed to shed some light on the MHD influence.

4.2.1. The one dimensional Stefan problem

In this test case, we consider the one dimensional Stefan problem which is widely used in validating the phase change models [17,28,29], as illustrated in Fig. 10. In this case, the liquid–vapor interface is initially at rest near the left end of the computational domain, which is viewed as a wall of constant temperature with $T = T_{wall}$, and the interface keeps at the saturating temperature during its motion. Initially, the temperature of the liquid phase is also assumed to be constant of T_{sat}, while the temperature in the vapor phase is linearly decrease within a difference of $T_{wall} - T_{sat} = 10$ K. The ratios of the physical properties between the two phases are $\frac{\rho_{liq}}{\rho_{vap}} = 1000$ and $\frac{\mu_{liq}}{\mu_{vap}} = 100$, the thermal diffusion coefficient is $\alpha = (\frac{\lambda}{\rho c_p})_{liq} = (\frac{\lambda}{\rho c_p})_{vap} = 0.025$ m^2/s, the thermal conductivity in the vapor phase is $\lambda_{vap} = 5 \times 10^{-3}$ W/(m K) and the latent heat is $h_{lg} = 10^4$ J/kg. The simulation is conducted in a domain with a global spatial resolution of $L \times L = 64 \times 64$, and cells near the interface is refined with two more levels.

Regarding such a problem, the exact solutions for the interface position and the temperature profile are derived in Ref. [47], given as

$$s_t = 2\zeta \sqrt{\alpha_{vap} t} \tag{47}$$

where s_t is the interface location at time t, α_{vap} the thermal diffusivity of the vapor phase, and ζ the solution to the transcendental equation

$$\zeta \exp(\zeta^2) erf(\zeta) = \frac{c_{p(vap)}(T_{wall} - T_{sat})}{h_{lg}\sqrt{\pi}} \tag{48}$$

where erf is the error function.

Fig. 11 shows the position of the interface versus time by using the present numerical model, respectively with and without setting the ghost cells outside the vapor phase. It is observed that through setting the ghost cells to keep the interface at $T_\Gamma = T_{sat}$, the numerical result agrees very well with the analytical solution. In contrast, without setting the ghost cells, the motion of the interface is faster than the analytical result, indicating that it is rather important to impose an accurate boundary condition for the temperature at the interface.

4.2.2. Two-dimensional bubble growth with a constant and uniform boiling rate

The second test case is about a two-dimensional static bubble growing with a constant phase change mass flow rate. To achieve this, the vapor bubble is set in a constant and linearly distributed temperature field, that is $T = T_0 + 1.0R$ where R being the radial distance from the domain center. The bubble initial radius is equal to $R_0 = 0.1$ m, and we consider the following physical properties, $\rho_{liq} = 1000$ kg/m^3, $\rho_{vap} = 1$ kg/m^3, $\sigma = 0.07$ kg/m^3, $\mu_{liq} = 10^{-3}$ kg/(m s), $\mu_{vap} = 1.78 \times 10^{-5}$ kg/(m s). This test is almost the same as proposed by Tanguy et al. [22], the only difference is that they impose a
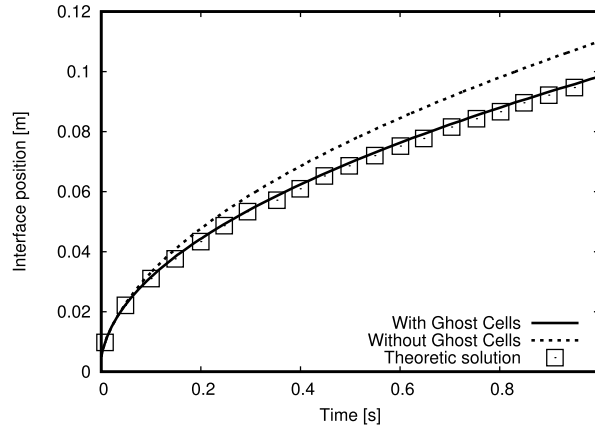
Fig. 11. Time history of the interface position for Stefan problem. Dashed line: without setting ghost cells; solid line: with setting ghost cells; square: analytical solutions.
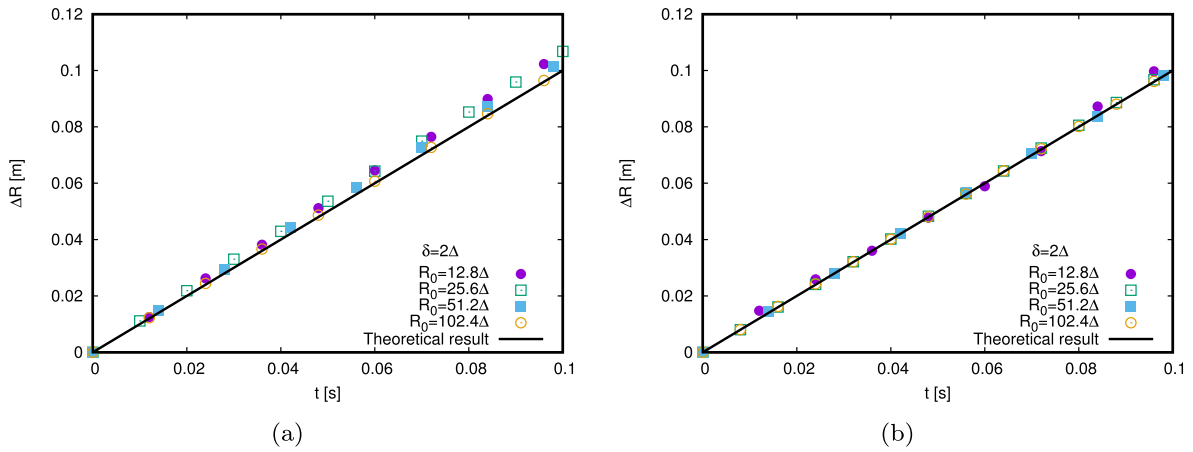

Fig. 12. Comparison of the bubble radius temporal evolution between analytical solutions and different numerical methods: (a) sharp scheme; (b) smooth scheme.

constant mass flows rate directly at the interface, and that value is tenth of that in the present study. Furthermore, by assuming the heat conductivity to be $\lambda_{liq} = 1$ W/(m K) and the latent heat is $h_{lg} = 1$ J/kg, the mass flow rate is calculated as $\dot{m} = \frac{(\lambda_{liq} \partial T / \partial R)}{h_{lg}} = 1$ kg/(m^2 s) if we only consider the heat flux from the liquid phase. Then the bubble radius will increase linearly with time:

$$R(t) = R_0 + \frac{\dot{m}}{\rho_{vap}} t \tag{49}$$

A convergence study has been performed about the artificial smearing of the mass source, firstly we use the sharp scheme by setting $\varepsilon = 0$ in Eq. (44). The second scheme is the smoothed method by setting $\varepsilon \neq 0$, and in addition, the thickness of the diffusion layer is set as $\delta = 2\Delta$, where Δ is the cell size at the interface. A comparison for the temporal evolution of the bubble radius increment between the two methods has been plotted in Fig. 12(a) and Fig. 12(b) at different levels of spatial discretization. It should be noted that the AMR technique is also adopted here that the grids in vicinity of the interface are refined with two more levels. From the figure, it is observed that with the sharp method, the numerical results do not collapse to the analytical solutions even with the spatial resolution of $R_0 = 51.2\Delta$, however with the smooth method, the numerical results already converges to the analytical solution at a spatial resolution of $R_0 = 25.6\Delta$. This result is different from what is reported by Tanguy et al. [22], who find the smoothed method with a Delta function would strongly produce an error, which is not decreased with grid refinement. In addition, a quarter of the bubble shape at different time instants, namely $t = 0.0, 0.02$ s, 0.04 s, 0.06 s, 0.08 s and 0.10 s, are presented in Fig. 13 on grids of $R_0 = 51.2\Delta$, the left one uses the sharp scheme while the right one is the smooth scheme. Beside, the red solid line in both figures indicates the analytical position of the bubble interface at $t = 0.1$ s. From the figure, it is more striking that by using a sharp method, the bubble can not preserve an axi-symmetric shape that the unphysical deformation becomes significant at $t = 0.2$ s, in contrast, the smooth method always keeps the bubble at an axi-symmetric shape even at the end of the simulation.
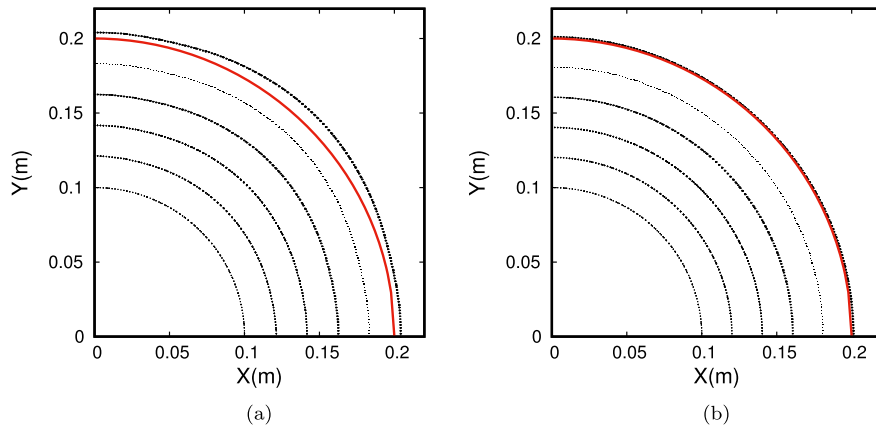
Fig. 13. The bubble interface positions at different time instants, respectively of $t = 0.0, 0.02\,s, 0.04\,s, 0.06\,s, 0.08\,s$ and $0.10\,s$ from inner to outside. For dotted lines: (a) sharp scheme; (b) smooth scheme, while the red solid line is the analytical position of the bubble interface at $t = 0.1\,s$.
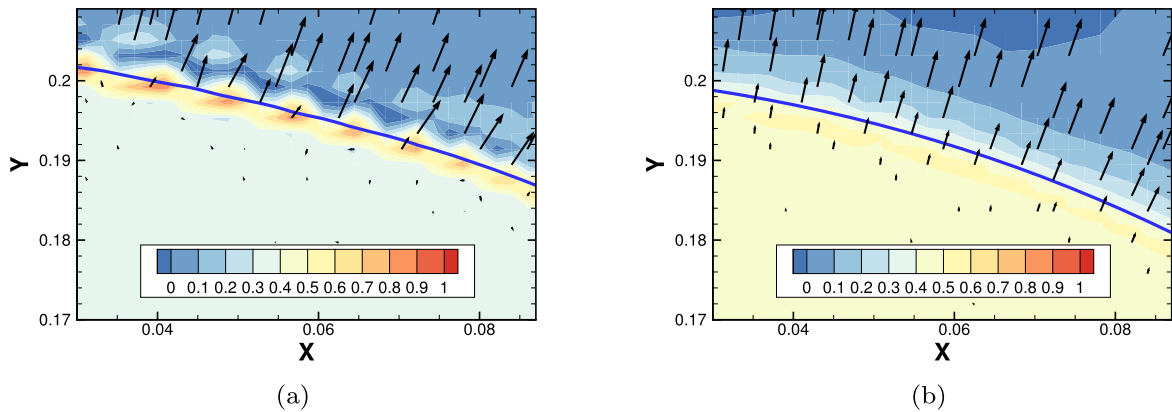
Fig. 14. Contour maps of the pressure field near the bubble interface, attaching with the velocity vectors. (a) Sharp scheme; (b) smooth scheme.

To detect why the sharp approach can not produce a good result, the contour maps of the pressure are presented in Fig. 14, where the left and right figures correspond to the sharp scheme and the smooth scheme, respectively. It is observed that the pressure field shows some oscillations by using the sharp method, while it is greatly improved by applying the smooth method. Besides, the velocity vectors are also plotted in the figure, some of the velocity vectors are not observed to be normal to the interface within the sharp scheme, and probably this causes the asymmetric expansion of the bubble shape. In order to decrease the numerical instabilities by using the sharp method, we have tried some numerical remedies. Such as by modifying the approximate projection method into an absolute projection method by solving an additional Poisson equation, as given by Ni [48]. However, even if the velocity field is fully divergence-free after the modification, the results are still not so satisfactory. Moreover, we have also tried another method proposed by Schlottke and Weigand [24], who use a corrected velocity at the interface to decrease the pressure oscillations, nevertheless, we still do not obtain more stable results. This asymmetric distribution is also found and discussed by Sato et al. [28] who also employ a VOF method to simulate the phase change flows, this asymmetry is thought to be linked to the spurious flows in vicinity of the bubble interface, however, no solution is found yet.

On the other hand, we also study the influence of the thickness of the artificial diffusion layer, while the spatial resolution is kept with $R_0 = 25.6\Delta$. The results are given in Fig. 15(a), it is noticed that with larger δ, the numerical solution is far worse by comparing with the analytical result, and moreover, the accurate solution is obtained with $\delta = 2\Delta$. In addition, the distribution of the mass source $\dot{m}$ before and after the smearing procedure are presented in Fig. 15(b) and Fig. 15(c) respectively, in which the sharp mass source is diffused into the neighbor cells after smoothing.

Through this test case, it is proved that the estimation of the temperature gradient at the interface is correct, and moreover, the smooth model is effective in stabilizing the numerical simulations.

4.2.3. Growing vapor bubble in a superheated liquid under zero gravity

The evaporating bubble expanding in a superheated liquid is analogous to the last test case of the vapor bubble growth with a constant and uniform boiling rate, however, the former one is much more challenging that a thin thermal boundary
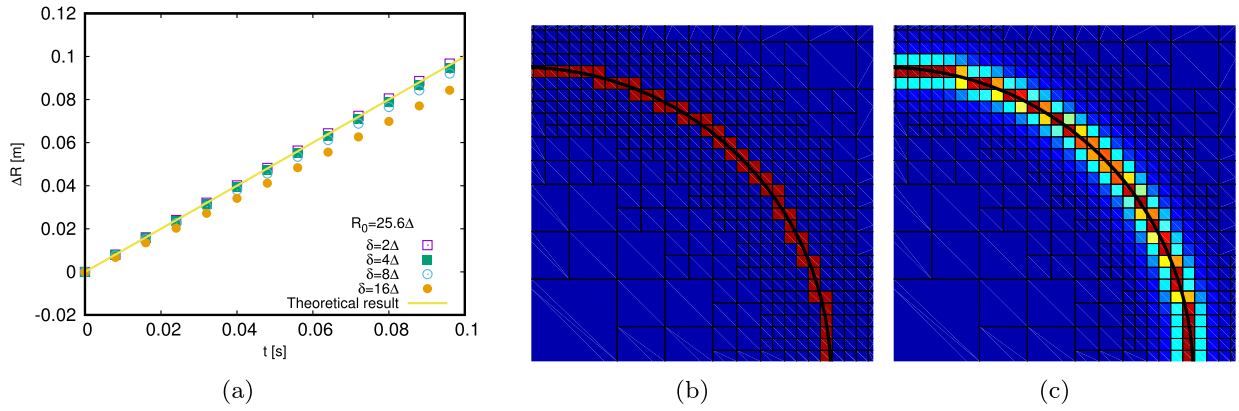
Fig. 15. (a) The influence of the thickness of the diffusion layer on the numerical results; (b) the sharp mass source before smearing; (c) the diffused mass source after smearing.

Table 1
Physical properties of water and ethanol at 101.3 kPa.

	Phase	ρ (kg/m³)	μ (Pa s)	c_p (J/kg K)	λ (W/m K)	h_{lg} (J/kg)	σ (N/m)	T_{sat} (K)
Water	vapor	0.597	1.26×10^{-5}	2030	0.025	2.26×10^{6}	0.059	373.15
	liquid	958.4	2.8×10^{-4}	4216	0.0679			
Ethanol	vapor	1.435	1.04×10^{-5}	1830	0.020	9.63×10^{5}	0.018	351.45
	liquid	757.0	4.29×10^{-4}	3000	0.154			

layer develops and forms in the liquid side close to the bubble interface. Correspondingly, the bubble expands in the amount determined by the heat flux from the liquid, as being analytically solved by Scriven [49] for a three-dimensional problem, and this solution is widely used to study the convergence of different numerical methods [28,22,18]. Recently, a similarity solution is derived by M.S. Lee et al. [50] for a cylindrical two-dimensional bubble case within the superheated liquid at $T_\infty = T_{sat} + \Delta T$, then the evolution of the bubble radius R is written as a function of time:

$$R = 2\beta_g \sqrt{\alpha_{liq} t} \tag{50}$$

where β_g is the "growth constant" obtained from

$$1 - 2\beta_g^2 \frac{\rho_{vap}}{\rho_{liq}} (\frac{1}{Ja} + \epsilon) exp(\beta_g^2) \int_0^1 (1 - \xi)^{1 - 2\chi\beta_g^2} exp\left(\frac{-\beta_g^2}{(1 - \xi)^2}\right) \frac{1}{(1 - \xi)^2} d\xi = 0 \tag{51}$$

where $\epsilon = 1 - \frac{c_{p(vap)}}{c_{p(liq)}}$, $\chi = 1 - \frac{\rho_{vap}}{\rho_{liq}}$ and Ja the non-dimensional Jakob number being $Ja = \frac{c_{p(liq)}(T_\infty - T_{sat})}{h_{lg}}$.

The analytical solution for the temperature T is:

$$\frac{T(s) - T_\infty}{T_{sat} - T_\infty} = 2\beta_g^2 \frac{\rho_{vap}}{\rho_{liq}} (\frac{1}{Ja} + \epsilon) exp(\beta_g^2) \int_{1 - \frac{\beta_g}{s}}^1 (1 - \xi)^{1 - 2\chi\beta_g^2} exp\left(\frac{-\beta_g^2}{(1 - \xi)^2}\right) \frac{1}{(1 - \xi)^2} d\xi \tag{52}$$

It should be noted that the influence of the gravity is not considered, which means the shape of the bubble should always keep circular during the evaporation in theory. Then simulations have been performed for the water properties given in Table 1, which are corresponding to the system pressure 101.3 kPa. The liquid superheat is fixed at $\Delta T = T_\infty - T_{sat} = 2$ K. The initial radius of the vapor bubble is set with $R_0 = 20$ µm, which corresponds to the analytic solution at $t = 0.023$ ms. In vicinity of the interface, the initial temperature field in the liquid is imposed according to the analytic solution. In addition, if the thermal boundary layer is defined by the temperature profile of $(T - T_{sat})/\Delta T < 0.99$, it is possible to obtain an estimation of the thermal boundary thickness as $\delta = 5.2$ µm at the initial stage. Herein, three different adaptive spatial resolutions are adopted to investigate the grid independence, corresponding to Level 13 with $\Delta_{min} \approx \delta/2$, Level 14 with $\Delta_{min} \approx \delta/4$ and Level 15 with $\Delta_{min} \approx \delta/8$, respectively, where Δ_{min} is the size of the smallest grid in vicinity of the bubble interface.

The comparison of the evolution of the bubble radius between the numerical result and the analytical solution is presented in Fig. 16. As expected, the computed results converge to the analytical solution as the grids are refined.
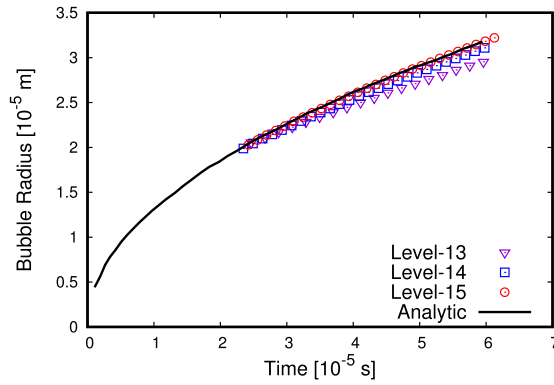
Fig. 16. Time evolution of bubble radius for evaporating three-dimensional bubble in superheated liquid ($\Delta T = 2$ K). The working fluid is saturated water at $P = 101.3$ kPa, and different spatial resolution levels correspond to $\Delta_{min} \approx \delta/2$, $\delta/4$ and $\delta/8$, respectively. δ is the thermal boundary thickness and Δ_{min} is the smallest mesh size in vicinity of the vapor bubble interface.


(a)   (b)
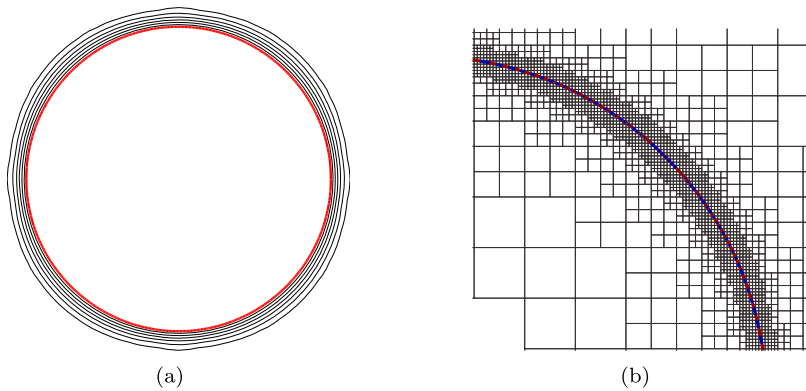
Fig. 17. (a) Temperature iso-lines (black) between $0 \sim 2$ K for the highest resolution case at $t = 60$ μs for the evaporating bubble in superheated liquid ($\Delta T = 2$ K), the interface of the evaporating bubble is depicted by the red solid line. (b) The fits between the isotherm line of $T = T_{sat}$ (blue dotted line) and the vapor bubble interface (solid red line). The spatial resolution is Level 15, corresponding to $\Delta_{min} \approx \delta/8$ close to the interface.

Fig. 17(a) shows the temperature iso-lines (black) between $0 \sim 2$ K for the highest resolution case at $t = 60$ μs, while the red line is the vapor bubble interface. It is found that the temperature distribution is radially symmetric close to the interface, though some slight asymmetry can be noticed in the peripheral area, where corresponds to $T - T_{sat} \approx 2$ K. This is because of the coarse meshes used there, corresponding to the size of $\Delta = 8\Delta_{min}$ in that region, as given in Fig. 17(b) for local zoom of the mesh distributions. However, such deformation does not influence the calculation of the mass transfer rate close to the interface. In Fig. 17(b), the isotherm line of $T = T_{sat}$ is plotted as the blue dotted line, while the vapor bubble interface is still represented by the red line. It is observed that the two lines fit very well, indicating that the saturated temperature is perfectly imposed at the bubble interface.

4.2.4. Rising vapor bubble in a superheated liquid under gravity and vertical magnetic fields

Based on the last test case without gravity, another three-dimensional vapor bubble rising in superheated liquid under gravity is then simulated as a further validation of the numerical method. This test is more complex since the bubble rises with the aid of gravity, then the inhomogeneous deformation and the expansion of the vapor bubble is coupled during its motion. Under such circumstance, both the mass transfer rate and the rising velocity of the bubble should be predicted accurately because the temperature field is convected by the coming flow. Fortunately, there are a series of experimental data obtained by Florchuetz et al. [51], and besides, some available numerical results [28,52] also provide us with benchmarks for such problems.

The working fluid is selected as vapor ethanol at a system pressure of 101.3 kPa, and the physical properties are also listed in Table 1. The liquid superheat is set at $\Delta T = 3.2$ K in the vast region far away from the bubble interface, while the temperature distribution close to the interface is given in the analytic formula of Eq. (52). The center of the vapor bubble, initially of radius $R_0 = 210$ μm corresponding to $t = 5.6$ ms, is located at 1.25 mm height from the bottom of the computational domain, which is almost $20R_0 \times 20R_0 \times 60R_0$. The thickness of the thermal boundary at the initial condition is 40.5 μm, and we still use the spatial resolution of Level 15 with almost 8 cells ($\Delta_{min} = \delta/8$) being located in the thermal boundary layer. In addition, the wake region behind the bubble, where the thermal convection is dominating, is refined to
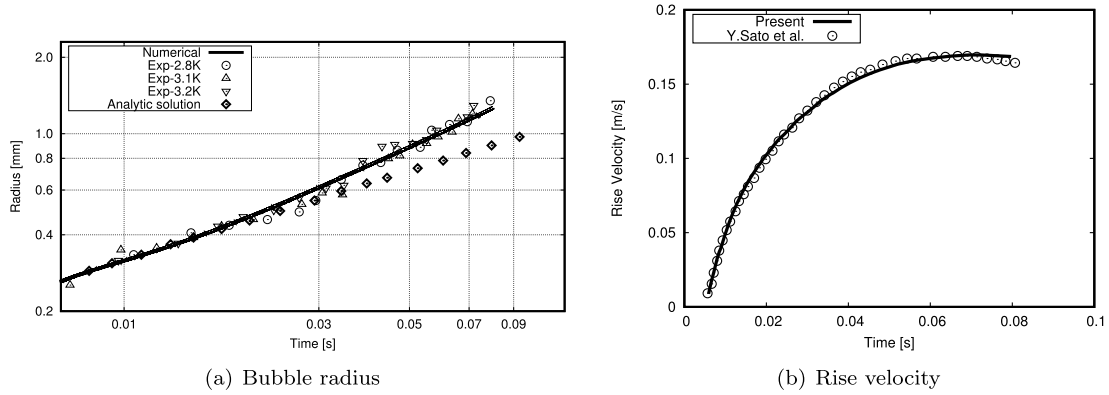
Fig. 18. (a) Comparison of bubble radius determined from the present computation, experimental measurement [51] and Scriven's analytical solution [49] with zero gravity as a function of time. (b) Comparison of the rise velocity of the bubble mass center from the present computation and the numerical results obtained by Sato et al. [28]. It is observed for both figures, the present numerical solutions agree well with the available references.

Level 13 by adopting the AMR technique if the gradient of temperature satisfies $\| \nabla T \| > 0.01$. It should be noted that the same test case is carried out by Sato et al. [28].

Different from the zero gravity case, the vapor bubble rising under gravity will show an obvious shape deformation from sphere to oblate ellipsoid in accompany with expanding volume, and hence the growth rate of the vapor bubble radius should be typically greater than the analytical solution given by Scriven [49]. With reference to the present study, the computed bubble radius as a function of time is plotted in Fig. 18(a), where the experimental data obtained under gravity [51] and the analytical solutions under zero gravity [49] are also given for comparison. The experimental data are correspondence to $\Delta T = 2.8$ K, 3.1 K and 3.2 K respectively, while the computed bubble radius is calculated according to the same way in experiments:

$$R = \frac{1}{2} \frac{(D_x + D_y)/2 + D_z}{2} \tag{53}$$

where D_x, D_y and D_z are the bubble diameters in the different directions, z being the rising direction.

In the figure, it is observed that at the initial stage when the shape of the vapor bubble is almost spherical, the simulation results, the analytical solution and the experimental data collapse to a single curve. However, as the vapor bubble deforms, progressively from $t \simeq 0.02$ when the shape deformation is obvious, the analytical solution can not predict the bubble radius well any longer, nevertheless the present numerical results are still in good agreement with the experimental data over the entire rising period. It should be kept in mind that the numerical solutions obtained by Sato et al. [28] also fit well with the experimental data, however they are not presented here to make the figure clean. In addition, the bubble rise velocity, which is calculated from the height of the mass center of the bubble, is also drawn in Fig. 18(b), and the numerical result by Sato et al. [28] is given for comparison. Good agreement is observed between them, indicating that the velocity field is also predicted accurately in the present simulation.

Besides, Fig. 19(a) shows the overall view of the bubble shape and the temperature distribution in the center vertical plane ($y = 0$) at $t = 0.079$ s. A region of lower superheat is observed beneath the bubble due to the wake effect of the bubble rising, and hence, the mass transfer rate at the rear of the bubble is typically less than that on the upper surface and the side of the bubble. Fig. 19(b) is the local zoom view close to the upper interface of the bubble, showing that at least 5 meshes are located inside the thermal boundary layer with the AMR technique. The velocity vectors are also plot herein.

After that, we would like to investigate the influence of the vertical magnetic field on the bubble rising during vaporization, it is in actual demand in designing the blanket component of the fusion devices since the vaporization of the liquid metal can be used to enhance the heat transfer under the MHD resistant effect, and consequently, it is important to know how the external magnetic fields affect the mass and heat transfer during vaporization. With reference to this problem, different vertical magnetic fields are imposed from $t = 0.018$ s after the vapor bubble already rises for a while, and the time series of the rise velocity of the vapor bubble are plot in Fig. 20(a). Note that the magnetic strengths are $B_z = 0.1$ T, 0.3 T and 0.8 T respectively, and the electric conductivity of the liquid is assumed to be $\sigma_e = 10^6$ S/m while the vapor phase is electrically insulating. If we define a variant interaction number in formulation of $N = \sigma_e B^2 R_0/(\rho \sqrt{g R_0})$, the three cases correspond to $N = 0.55$, $N = 1.53$ and $N = 6.12$, respectively.

It is observed that under vertical magnetic fields, the rise velocity of the vapor bubble is significantly decreased, and this is consistent with what we obtain for a non-evaporation bubble [7] in presence of a vertical magnetic field. That is, the induced Lorentz forces tend to suppress the motion of a rectilinearly rising bubble. In another aspect, as shown in Fig. 20(b), the expanding of the bubble radius is also suppressed under stronger magnetic fields. This is mainly because the shape deformation of the bubble is less striking under such circumstance, and moreover, the evolution of the bubble

(a) Overall view
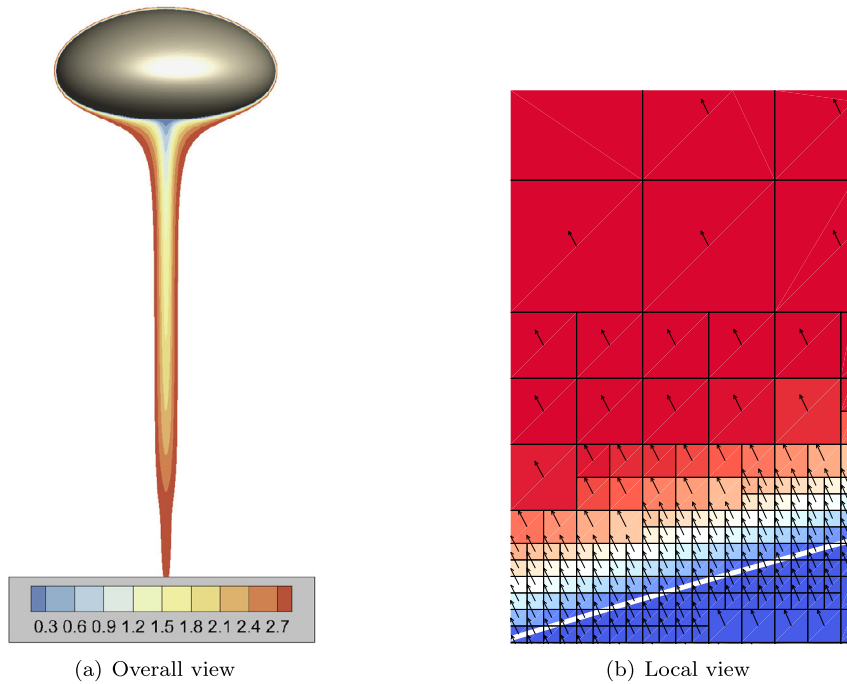
(b) Local view

Fig. 19. Bubble shape and distributions of temperature difference at $t = 0.079$ s. (a) The overall view of the whole computational domain; (b) the local view in vicinity of the upper interface of the bubble, the vectors are the velocity field and the temperature contour levels are identical with (a).

(a) Rise velocity
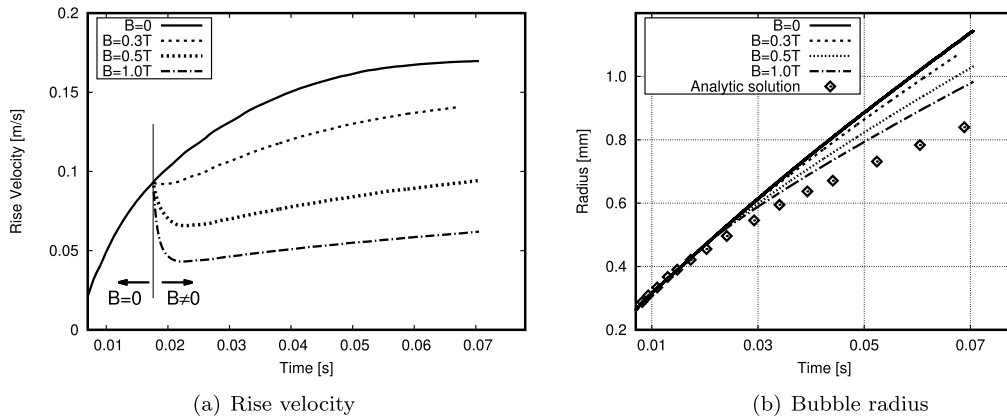
(b) Bubble radius

Fig. 20. The influence of the external magnetic fields on the vapor bubble motion, while different magnetic fields are turned on at $t = 0.018$ s. (a) The time histories of the rise velocity; (b) the time histories of the bubble radius.

radius tends to collapse to the analytical solution with a more spherical shape. For the time histories of the bubble shapes in the vertical center plane, they are also displayed in Fig. 21 under different magnetic fields, while the time instants are $t = 0.018$ s, $t = 0.028$ s, $t = 0.038$ s, $t = 0.048$ s, $t = 0.058$ s and $t = 0.068$ s respectively. It is observed that under stronger magnetic fields, the shape deformations of the bubble are typically smaller, and correspondingly, the expanding of the bubble volume due to mass transfer is also decreased.

On the other hand, as to the heat transfer rate, Nusselt number is the typical dimensionless parameter to define the ratio between the thermal flux and heat conduction at the bubble interface, given as

$$Nu = \rho_{vap} h_{lg} \frac{dR}{dt} \frac{2R}{\lambda_{liq}(T_\infty - T_{sat})} \tag{54}$$

Accordingly, the heat transfer rate depends on both the growth rate and the value of the bubble radius. Because the magnetic fields suppress the bubble expansion, and hence the heat transfer rate is also expected to be deceased.

Another issue deserves attention is that if the electric conductivity of the vapor bubble can not be ignored in comparison with the superheat liquid, the rising behaviors of the bubble are expected to be different between a more conducting bubble
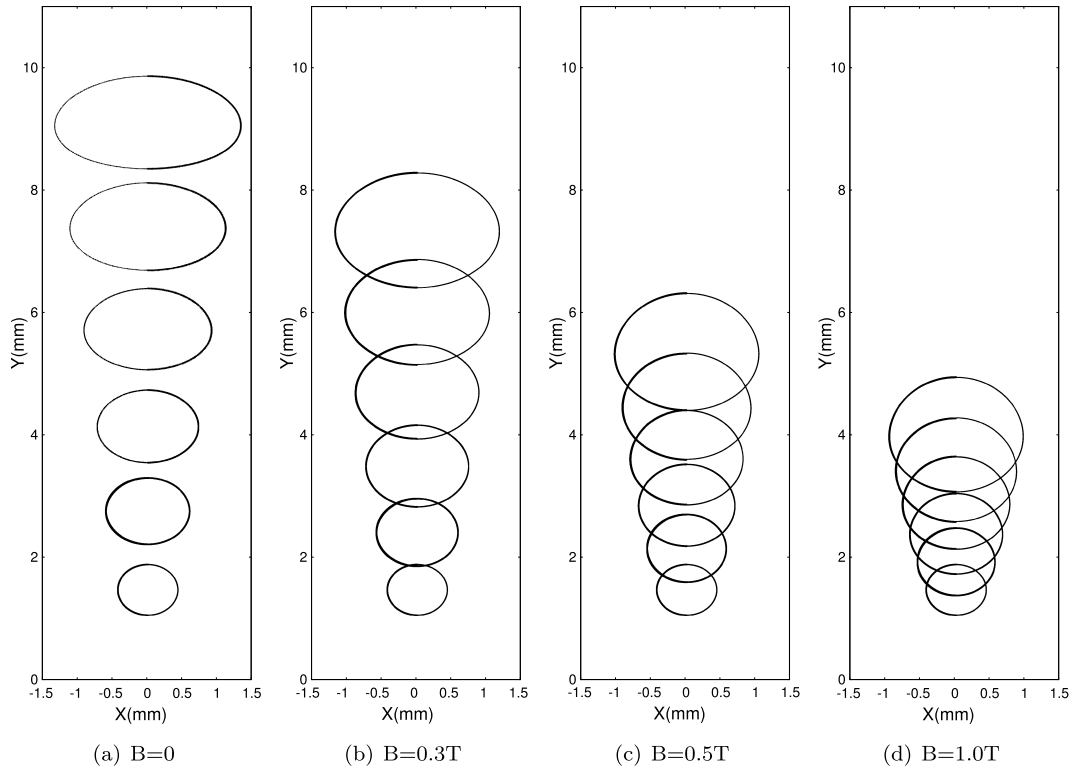
Fig. 21. The evolutions of the bubble shapes under different magnetic fields, respectively of (a) $B = 0$, (b) $B = 0.3$ T, (c) $B = 0.5$ T and (d) $B = 1.0$ T. The time instants in each figure correspond to $t = 0.018$ s, 0.028 s, 0.038 s, 0.048 s, 0.058 s and 0.068 s, respectively. It is observed that with stronger magnetic field, the bubble deformation is smaller.
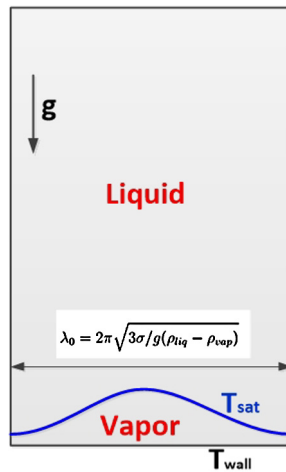

Fig. 22. The schematic diagram of the two dimensional film boiling flows.

and a less conducting bubble. Similar study has been carried out to investigate the droplet motion exposed to an external electric field [53], and the electric conductivity of the droplet is found to be rather important in determining the droplet migration behaviors. Nevertheless, such investigations are beyond the scope of the present manuscript while they will be researched more thoroughly in the following study.

4.2.5. Two-dimensional film boiling flows

In this test case, we turn to the two-dimensional film boiling flows. The problem is illustrated in Fig. 22 that a thin layer of vapor phase is below the liquid and above a heated solid surface. The vapor film is initially defined by a function of cosine wave
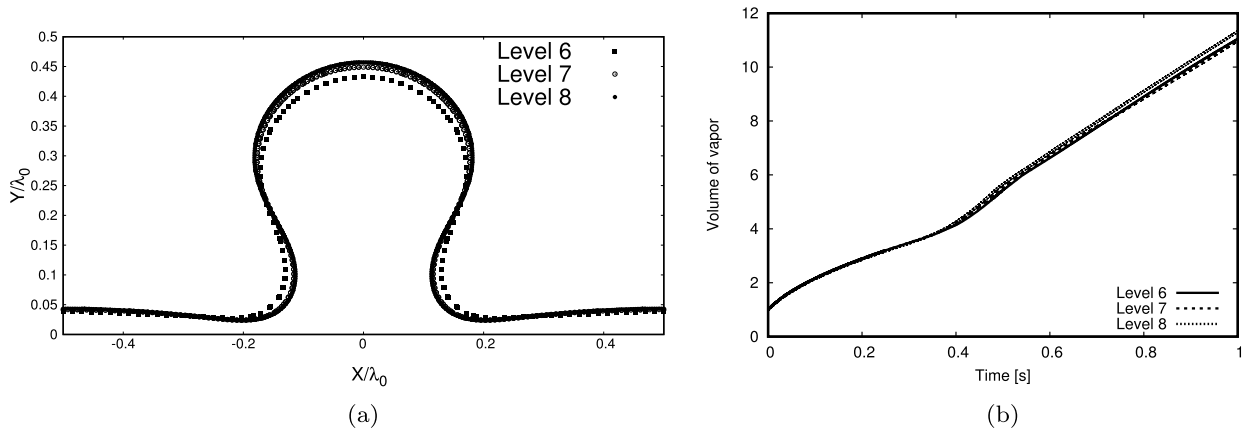
Fig. 23. The grid independence study of the film boiling flow under different spatial resolutions. (a) The bubble shape at $t = 0.45$ s; (b) the volume of the vapor bubble over time.

$$y = \frac{\lambda_0}{128}(4.0 + cos(\frac{2\pi x}{\lambda_0})) \tag{55}$$

where λ_0 is the most unstable Taylor wavelength, given as

$$\lambda_0 = 2\pi \sqrt{3\sigma / g(\rho_{liq} - \rho_{vap})} \tag{56}$$

The initial shape of the vapor film will promote the onset of Rayleigh–Taylor instability by gravity. With the evaporation of the liquid and the generation of the fresh vapor near the wall, the liquid is prevented from contacting with the wall and the vapor bubble is formed at the crest of the wavy interface. The computational domain is taken the dimension of $\lambda_0 \times 3\lambda_0$. The bottom wall is set with a constant temperature of T_{wall}, and both the side walls are symmetrical boundary conditions, at the top of the computational domain a outflow boundary condition is imposed.

The physical parameters considered in the present study are as follows: the vapor parameters are $\lambda_{vap} = 1.0$ W/(m K), $\mu_{vap} = 5 \times 10^{-3}$ Pa s, $c_{p(vap)} = 200$ J/(kg K) and $\rho_{vap} = 5$ kg/m^3, whereas the liquid properties are $\lambda_{liq} = 40.0$ W/(m K), $\mu_{liq} = 0.1$ Pa s, $c_{p(liq)} = 400$ J/(kg K) and $\rho_{liq} = 200$ kg/m^3. Surface tension coefficient is $\sigma = 0.1$ N/m, latent heat is $h_{lg} = 10^4$ J/kg, and the temperature difference between the wall of the interface is $T_{wall} - T_{sat} = 5$ K. This test case was proposed by Welch and Wilson [54], and then reproduced by some other researchers [17,55,56].

Firstly, the grid independence study is conducted with different spatial resolutions, respectively of Level 6 of 64×192, Level 7 of 128×512 and Level 8 of 256×768. It should be noted that the AMR technique is used here to save the computational resources, and hence Level 6 (7, 8) implies the finest grid close to the interface, otherwise, the grids are much coarser in other bulk regions. At $t = 0.45$ s, the shapes of the vapor bubble under different spatial resolutions are given in Fig. 23(a), in addition, Fig. 23(b) depicts the vapor volume relative to the initial vapor volume over time. Both figures indicate that Level 7 is fine enough to simulate the film boiling flows. Therefore, we use this grid to conduct the following simulations.

Besides, to validate that the liquid–vapor interface keeps at the saturating temperature during the film boiling, the isoline of $T = T_{sat}$ is plotted as the red line in Fig. 24, while the black line is the position of the interface. As shown in the figure, the two lines almost coincide with one another, indicating that the saturating temperature is imposed accurately at the liquid–vapor interface.
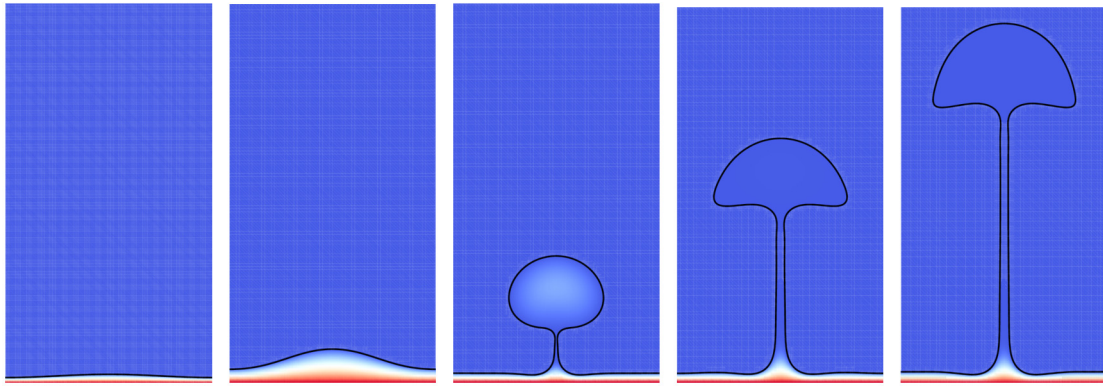
Moreover, the evolution of the bubble shapes at different time instants is presented in Fig. 25, respectively at $t = 0$ s, $t = 0.3$ s, $t = 0.5$ s, $t = 0.7$ s and $t = 0.9$ s. In the figures, the vapor bubble grows due to the vaporization at the liquid–vapor interface, however, we do not observe the bubble to detach from the thin vapor film even at $t = 0.9$ s. Instead, a long and thin stem is observed to connect the bubble and the film. This result is contrary with many other studies [29,56,54], most of which report that a quasi-steady bubble release pattern would be appeared. The "vapor jet" behavior observed here seems to be surprising. But according to Gibou et al. [55] who simulate the film boiling with the GFM, they also find the bubble does not pinch off and the vapor bubble persist. They think this to be qualitatively correct for a two-dimensional simulation because "*the curvature for the stem is close to zero and therefore the effects of surface tension are negligible*", and therefore no bubble is released from the thin film. In addition, some other studies [17,30] also confirm the bubble not to detach from the thin film in two dimensional simulations. Again by Gibou et al. [55], they predict the pinch-off mechanism is reasonable in three-dimensional cases, and this will be validated in our following test cases.

Regarding the heat transfer characteristics of the film boiling, the most important dimensionless number is Nu, which describes the ratio between the heat convection and the heat conduction, being defined as
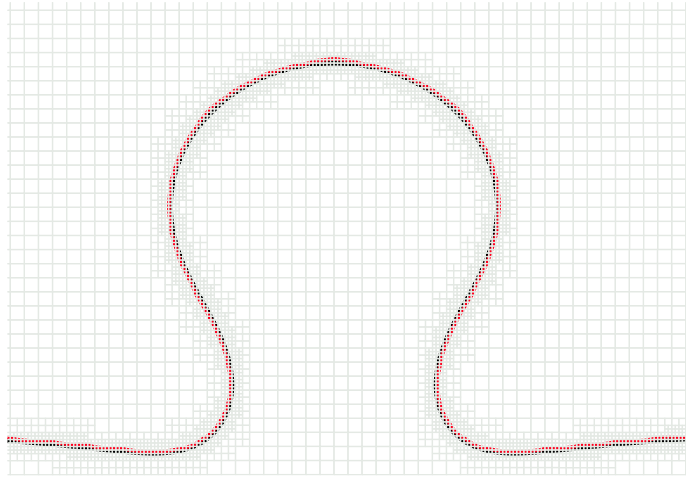
Fig. 24. The isoline (red) of $T = T_{sat}$ and the interface (black) of the vapor bubble at $t = 0.45$ s. It is observed that the two lines almost coincide with one another, indicating that the saturating temperature is imposed accurately at the liquid–vapor interface.

Fig. 25. The evolution of the bubble shapes during the film boiling flow. From left to right: $t = 0$ s, $t = 0.3$ s, $t = 0.5$ s, $t = 0.7$ s and $t = 0.9$ s. The bubble does not detach from the thin film, and this observation is consistent with some available studies [55,17,30].

$$Nu = \frac{1}{L} \int_0^L \frac{\lambda'}{T_{wall} - T_{sat}} \frac{\partial T}{\partial n}|_{wall} dx \tag{57}$$

where L is the length of the bottom wall, being λ_0 in the present study. $\lambda' = \lambda_0/2\sqrt{3}\pi$ is the characteristic length, and $\partial T/\partial n$ is the temperature gradient at the bottom wall.

Klimenko [57] developed semi-empirical models on a horizontal surface to predict Nu in the film boiling flows, and they are widely used as analytical solutions. For the current case, the correlation proposed by Klimenko is given as

$$Nu_k = 0.019(GrPr)^{1/3} \tag{58}$$

where Gr and Pr are the Grashof number and the Prandlt number, respectively. They are defined as

$$Gr = \frac{\rho_{vap}(\rho_{liq} - \rho_{vap})g\lambda'^3}{\mu_{vap}^2}$$
$$Pr = \frac{c_{p(vap)}\mu_{vap}}{\lambda_{vap}} \tag{59}$$

Fig. 26 shows the comparison between the numerical result (Eq. (57)) and the analytical solution (Eq. (58)). It is observed that even on the coarsest grids, the numerical result still agrees well with the prediction by Klimenko. In addition, because no bubble pinches off during the film boiling, we do not observe the Nu to oscillate over time, and it converges to Nu_k on all spatial resolutions. The evolution tendency of Nu is consistent with Akhtar and Kleis [30], who also indicate that Nu will not show periodic oscillations but converges to the analytical solution.
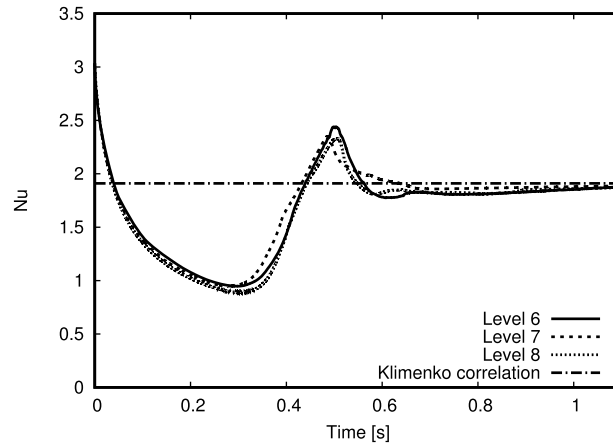
Fig. 26. The evolution of Nu under different spatial resolutions, the correlation by [57] is also presented for comparison. It is observed that all the numerical results converge to the analytic solution without periodic oscillations.
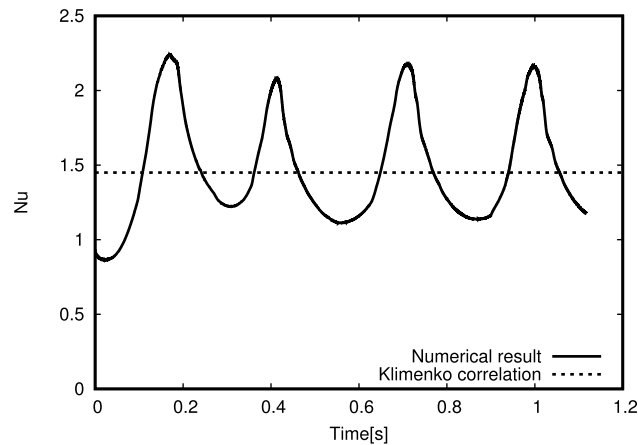
Fig. 27. The evolution of Nu in the three-dimensional film boiling flows. It is observed that the numerical result almost oscillates around the analytical solution, indicating that the bubbles are periodically released from the thin film.

4.2.6. Three-dimensional film boiling with and without magnetic field

As shown by some available publications [22,28], the three-dimensional direct numerical simulations of the film boiling flows are very complex because it is delicate to keep the bubble growth in an axisymmetric manner. More importantly, we would like to test the validity of the solver by coupling the phase change model with the MHD computations.

For purpose of simplicity, the fluid properties are set as the same as those in the two-dimensional simulations, except that the temperature difference between the wall and the liquid–vapor interface is increased to $\Delta T = 10$ K, while the initial position of the vapor film is defined as $z = \frac{\lambda_0}{20}(2.5 + cos(\frac{2\pi x}{\lambda_0}) + cos(\frac{2\pi y}{\lambda_0}))$ and the initial temperature field is also linearly distributed from the wall (T_{wall}) to the interface (T_{sat}). It is known that the most dangerous wavelength is $\sqrt{2}\lambda_0$ for the three dimensional case [58,26], however, since Tsui et al. [29] show that it still make sense to set the width of the film as λ_0 in three-dimensional simulations, therefore, the computational domain is given as $\lambda_0 \times \lambda_0 \times 2\lambda_0$ in this test case. In addition, the grids near the interface is refined to Level 7, which is already proved to be adequate in simulating the film boiling flows.

Without the magnetic field, the evolution of Nu over time is plotted in Fig. 27, and still the Klimenko correlation is shown for comparison that a good agreement is observed between them. The figure clearly shows that the Nusselt number oscillates around the analytical solution, and correspondingly, the bubbles are expected to release from the thin film in a quasi-steady periodic pattern. As being very different from the two-dimensional film boiling case, however, it is consistent with the conclusion drawn by Gibou et al. [55], who think that the vapor bubble would just pinch off in the three-dimensional case due to the principal curvature of the stem.

In order to illustrate the periodic release of the vapor bubble during the film boiling, the evolution of the bubble shapes at different time instants is presented in Fig. 28, from $t = 0.72$ s to $t = 1.00$ s as a cycle. From $t = 0.72$ s to $t = 0.75$ s, a bubble is found to be ready to detach that the thin film is nearly flat during this time period. After the bubble is released
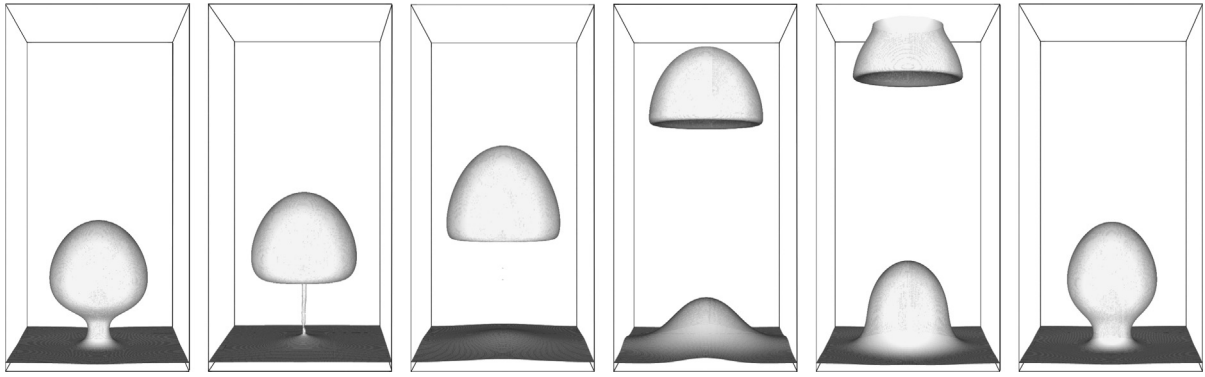
Fig. 28. The rising and releasing of the vapor bubble during the film boiling flow. From left to right: $t = 0.72$ s, $t = 0.75$ s, $t = 0.80$ s, $t = 0.91$, $t = 0.96$ s and $t = 1.00$ s. The bubble is observed to detach from the thin film at the time instance of $t = 0.75$ s, and after that, a new vapor bubble is formed subsequently at the bottom of the liquid.

from the thin film at the instant of $t = 0.80$ s, there are actually several small dimples formed at the film center due to the breaking up of the thin stem. However, we remove them artificially in order to preserve the stability of the numerical simulations. It should be also noted that this pinch off process can still be identified by further refining the grids to Level 8, and therefore it is not because of the inadequate spatial resolution. From $t = 0.91$ s to $t = 1.00$ s, the new vapor bubble is observed to grow from the thin film and a new cycle for the bubble to detach is starting.

After validating the capability of the model in simulating the phase change flows, we impose external magnetic fields for more complex numerical computations, where multiphysical fields are coupled together. External magnetic fields are imposed in either the vertical direction or the horizontal direction in order to investigate the MHD effect. The electric conductivities are set as $\sigma_{e(liq)} = 4 \times 10^5$ S/m and $\sigma_{e(vap)} = 0.1$ S/m while the magnetic intensities are varied with $B = 0.1$ T, $B = 0.3$ T and $B = 0.5$ T in both directions. If we define a variant interaction number of $N = \sigma_{e(liq)} B^2 \lambda' / \rho_{liq} \sqrt{g\lambda'}$ to describe the ratio between the Lorentz force and the gravitational force, it is possible to obtain the corresponding dimensionless value of $N = 0.54$, $N = 4.89$ and $N = 13.58$, respectively. Due to the limitation of the computational resources, the simulations are stopped after one period of the bubble releasing, and the results can already shed some light to the MHD influence on the boiling film flows.

The growing process of the first vapor bubble at different time instants are presented in Fig. 29 and Fig. 30, respectively for the vertical magnetic fields and the horizontal magnetic fields. In each group of the figures, the top row is the results without imposing magnetic field, while the other three rows correspond to the results of $B = 0.1$ T, $B = 0.3$ T and $B = 0.5$ T, respectively. In addition, from left to right, the time instants are $t = 0.05$ s, $t = 0.1$ s, $t = 0.15$ s. $t = 0.20$ s and $t = 0.23$ s. As shown in Fig. 29 where the vertical magnetic fields are imposed, the instant for the bubble to detach is delayed with a stronger magnetic field. For instance, the bubble is ready to detach at $t = 0.23$ s without a magnetic field, however, it still connects with the thin film in case of $B = 0.5$ T. This is well understood that as shown in our previous study [7], the Lorentz force in vicinity of the lower part of the bubble directs outwards from the bubble center, and it cancels out a part of the pressure difference across the interface of the bubble, therefore, the surface tension there is decreased for a balanced effect that the stem is more difficult to break up. Moreover, the bubble is elongated in the vertical direction, and this is also consistent with the previous result [7], it is still resulted from the redistribution of the pressure field around the upper side and the lower side of the bubble. On the other hand, in Fig. 30 where horizontal magnetic fields are imposed, the most striking characteristic of the MHD influence is that the boiling film flow tend to be two dimensional along the direction of the magnetic field. This transition is already obvious under $B = 0.3$ T and is fully completed in case of $B = 0.5$ T, by which we do not observe a spherical-like bubble to form from the thin film but a cylinder-like bubble is very conspicuous at $t = 0.23$ s. This is also consistent with some available studies, whatever the theoretic analysis [59,60] or the numerical simulations [8]. They all indicate that with a horizontal magnetic field, the flow structure would be more uniform along the direction of the magnetic field, and finally the flow tends to be two dimensional.

Then the evolution of the Nusselt number under different magnetic fields are also investigated, as presented in Fig. 31. In both figures, it is observed that the oscillation of the space-averaged Nu is weakened, indicating that the thin film is more stable under the influence of magnetic field because Nu is directly related to the thickness of the thin film. In addition, the space-averaged Nu seems to increase with B in either direction, that is probably because the thickness of the thin film is thinner with a stronger magnetic field. To be particular, under the horizontal magnetic field of $B = 0.5$ T, the developing trend of Nu is nearly flat over time because the film boiling becomes two dimensional and the bubble will not detach from the thin film.

Lastly, the streamlines of the current density in vicinity of the vapor bubble are plotted in Fig. 32, the left one refers to the vertical magnetic field while the right one is the horizontal field. The magnetic intensity is $B = 0.3$ T and the time instant is $t = 0.18$ s. In both figures, closed loops of the current density are observed closed to the interface, indicating that the computation of the current density is conservative in our numerical simulations. Although the streamlines of the
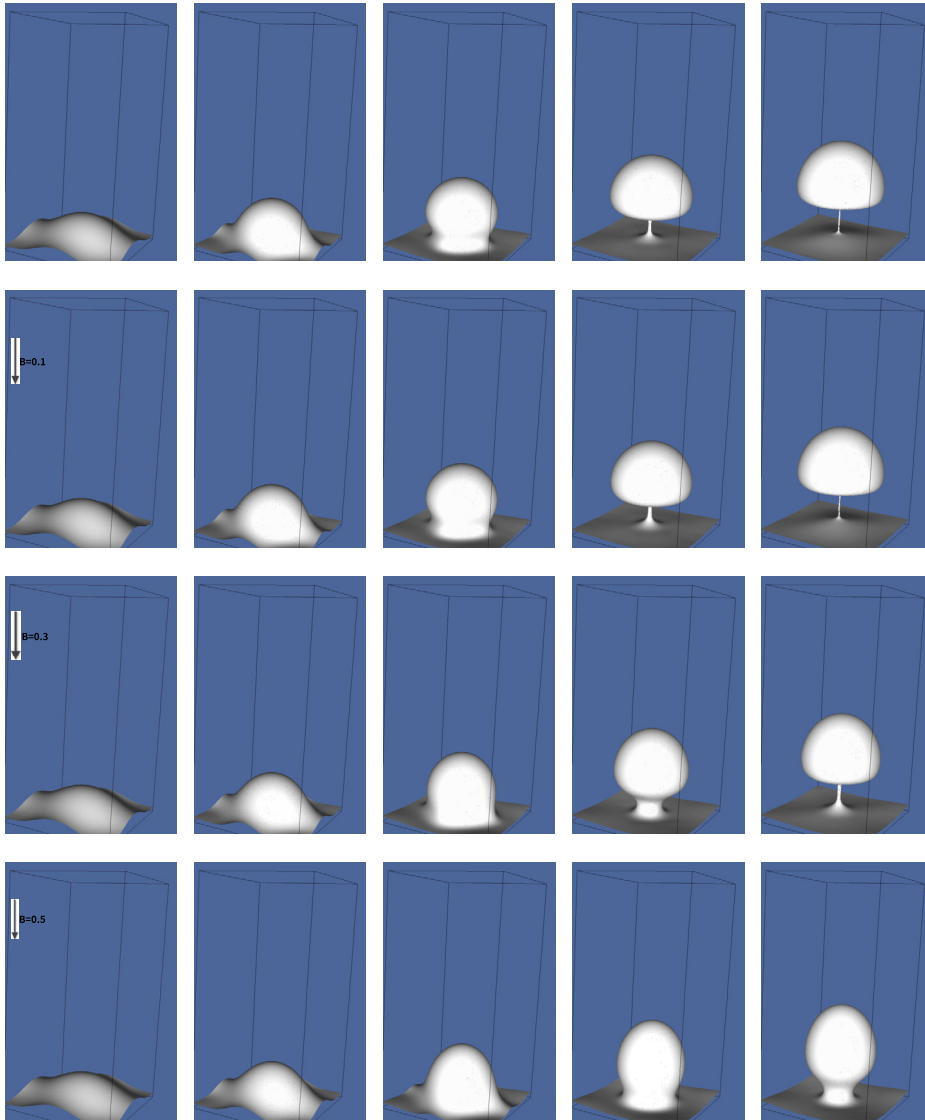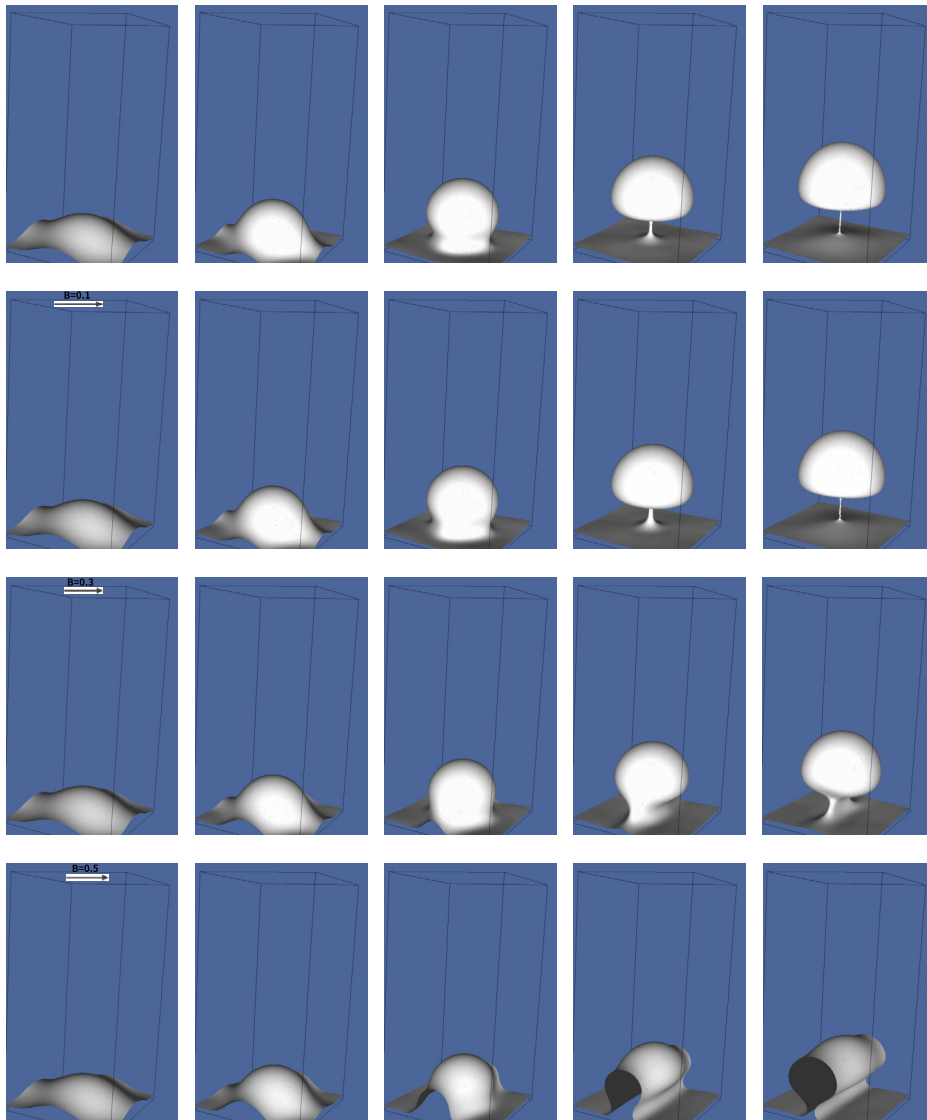
Fig. 29. The evolution of the bubble shapes during the film boiling flow without and with the vertical magnetic fields. From left to right: $t = 0.05$ s, $t = 0.10$ s, $t = 0.15$ s, $t = 0.20$ s and $t = 0.23$ s. From the top to the bottom row: $B = 0.0$ T, $B = 0.1$ T ($N = 0.54$), $B = 0.3$ T ($N = 4.89$), $B = 0.5$ T ($N = 13.58$). The time instant for the bubble to detach is delayed with stronger magnetic field, and the bubble is elongated in the vertical direction.

current density in the horizontal magnetic field seem to be not closed but ended at the domain boundary, however, it is because we use a slip boundary condition for the velocity field and therefore the current density is able to pass through the boundary.

5. Conclusion

In the present study, a new phase change model has been proposed for the simulation of incompressible multiphase magnetohydrodynamics based on the VOF method. The method is implemented in an incompressible multiphase MHD solver developed in our previous work [3]. Actually, the evaluation of the impacts of magnetic field on various stable-boiling regimes is in urgent demand in the design of the thermonuclear fusion device. Nevertheless to the best of the authors' knowledge, the present study is the first work in such multiphysics modeling, where the flow field, the temperature field, the electromagnetic field and the interface mechanics with phase change are coupled.

Before proposing the phase change model within the multiphase MHD flows, we reinvestigate the accuracy of the volume averaged scheme in estimating the electric conductivity in the mixed cells. Since it is rather important to conserve the current density inside the electrically conducting fluids, consequently, a cut-cell approach is introduced to capture the jump condition across the interface in computing the electromagnetic field. Owing to the piecewise linear reconstructed scheme

Fig. 30. The evolution of the bubble shapes during the film boiling flow without and with the horizontal magnetic fields. The descriptions are the same as those in Fig. 29. The growth of the bubble tends to be two dimensional with stronger magnetic field.

for the interface, the position and the normal vectors of the interface can be calculated sharply, and therefore, the internal boundary condition for the electric potential can be imposed on the interface sharply instead of using the volume averaged scheme. After performing a series of numerical tests, we find the proposed cut-cell method can keep the second-order accuracy during solving the Poisson equations with the Neumann boundary condition. We also demonstrate that even if the interface is translating or deforming with the flow, accurate solutions are still obtained based on the time-dependent reconstructed interface.

More important, for the frequently encountered phase change flows in the fusion engineering, where the MHD effect is rather significant, a phase change model is then proposed and validated. In the present model, the heat flux across the interface is calculated directly from the gradient of temperature in the liquid side and the vapor side respectively, while the interface is kept at the saturated temperature with a variant ghost cell method. This model has been verified for two linear one-dimensional phase change problems, often referred to as the Stefan problem and the vapor bubble growing in a superheated liquid with constant temperature gradient. The computed results agree well with the theoretical values, indicating that the mass flux is estimated accurately and the saturated temperature is fully imposed at the liquid–vapor interface. A two-dimensional verification case of a growing vapor bubble in a superheated liquid under zero gravity is also simulated, it is found that the bubble shape as well as the temperature distribution still keeps an radially symmetric distribution, and besides, the bubble growth rate still agrees well with the analytical solution. Furthermore, if the three-dimensional vapor bubble grows under gravity in a superheated liquid, it is found the bubble shape is no longer spherical because of the buoy-
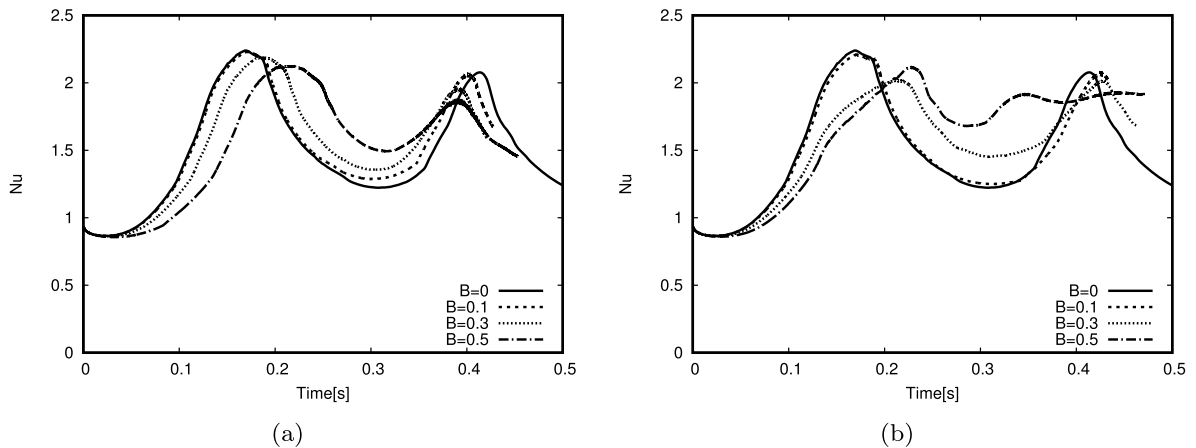
Fig. 31. The evolution of the Nusselt number over time under different magnetic fields. (a) Vertical magnetic field; (b) horizontal magnetic field.
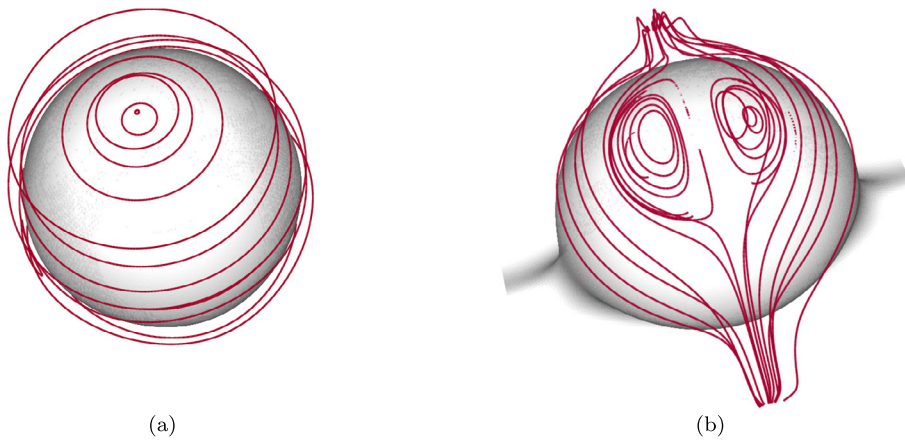
Fig. 32. The distribution of the streamlines of the current density around the bubble during its growth. The magnetic intensity is $B = 0.3$ T and the time instant is $t = 0.18$ s. (a) Vertical magnetic field; (b) horizontal magnetic field.

ancy, and good agreement is obtained for the growth rate of the bubble between the computations and the experiments. What is more, we also investigate the influence of the magnetic fields on the vapor bubble growth under gravity, it is found the growth rate as well as the bubble deformation is greatly suppressed by the magnetic fields. Then, for a more complex test of the two-dimensional boiling film flow, the predicted space-averaged Nusselt number is in good agreement with the analytical solution. However, we do not observe the bubble to release from the thin film and this is consistent with the result by Gibou et al. [55]. At last, the three dimensional numerical simulations are conducted about the boiling film flows under the influence of the magnetic field. Without the magnetic field, we find the bubbles to periodically detach from the film, and this is very different from the two dimensional case. By imposing the magnetic fields of different directions, the vapor bubble is elongated along the direction of the magnetic field, and the time for the bubble detaching is delayed with a stronger magnetic field.

With reference to the numerical algorithms proposed in this paper, they are still deserving of improvements in simulating the liquid metal phase change problems, such as to consider the oxidized interface and to estimate the temperature condition at the interface if the heat flux is extremely high.

Acknowledgments

References

[1] H. Bai, B.G. Thomas, Bubble formation during horizontal gas injection into downward-flowing liquid, Metall. Mater. Trans. B 32 (2001) 1143–1159.

[2] N.B. Morley, S. Smolentsev, L. Barleon, I.R. Kirillov, M. Takahashi, Liquid magnetohydrodynamics: recent progress and future directions for fusion, Fusion Eng. Des. 51 (2000) 701–713.

[3] J. Zhang, M.-J. Ni, Direct simulation of multi-phase MHD flows on an unstructured Cartesian adaptive system, J. Comput. Phys. 270 (2014) 345–365.

[4] S. Popinet, An accurate adaptive solver for surface-tension-driven interfacial flows, J. Comput. Phys. 228 (2009) 5838–5866.

[5] M.-J. Ni, R. Munipalli, N.B. Morley, P. Huang, M.A. Abdou, A current density conservative scheme for incompressible MHD flows at a low magnetic Reynolds number. Part I: on a rectangular collocated grid system, J. Comput. Phys. 227 (2007) 174–204.

[6] J. Zhang, M.-J. Ni, A consistent and conservative scheme for MHD flows with complex boundaries on an unstructured Cartesian adaptive system, J. Comput. Phys. 256 (2014) 520–542.

[7] J. Zhang, M.-J. Ni, Direct simulation of single bubble motion under vertical magnetic field: paths and wakes, Phys. Fluids 26 (2014) 102102.

[8] J. Zhang, M.-J. Ni, R. Moreau, Rising motion of a single bubble through a liquid metal in the presence of a horizontal magnetic field, Phys. Fluids 28 (2016) 032101.

[9] J. Zhang, M.-J. Ni, What happens to the vortex structures when the rising bubble transits from zigzag to spiral?, J. Fluid Mech. 828 (2017) 353–373.

[10] J.-J. Wang, J. Zhang, M.-J. Ni, R. Moreau, Numerical study of single droplet impact onto liquid metal film under a uniform magnetic field, Phys. Fluids 26 (2014) 122107.

[11] J. Zhang, T.-Y. Han, J.-C. Yang, M.-J. Ni, On the spreading of impacting drops under the influence of a vertical magnetic field, J. Fluid Mech. 809 (2016) R3.

[12] M.A. Abdou, A. Ying, N. Morley, K. Gulec, S. Smolentsev, M. Kotschenreuther, S. Malang, S. Zinkle, T. Rognlien, P. Fogarty, et al., On the exploration of innovative concepts for fusion chamber technology, Fusion Eng. Des. 54 (2) (2001) 181–247.

[13] C. Wong, L. Barlcon, M. Corradini, P. Fogarty, N. Ghoniem, S. Majumdar, S. Malang, R. Mattas, K. McCarthy, B. Merrill, et al., Evaluation of the tungsten alloy vaporizing lithium first wall and blanket concept, Fusion Technol. 39 (2P2) (2001) 815–822.

[14] L. Wagner, P. Lykoudis, Effect of liquid inertia on bubble growth in the presence of a magnetic field, in: AIChE Symp. Ser., vol. 73, United States, Purdue Univ., West Lafayette, IN, 1977.

[15] L.Y. Wagner, P.S. Lykoudis, Mercury pool boiling under the influence of a horizontal magnetic field, Int. J. Heat Mass Transf. 24 (4) (1981) 635–643.

[16] M. Takahashi, A. Inoue, T. Kaneko, Pool boiling heat transfer of mercury in the presence of a strong magnetic field, Exp. Therm. Fluid Sci. 8 (1) (1994) 67–78.

[17] S. Hardt, F. Wondra, Evaporation model for interfacial flows based on a continuum-field representation of the source terms, J. Comput. Phys. 227 (2008) 5871–5895.

[18] C. Kunkelmann, P. Stephan, CFD simulation of boiling flows using the volume-of-fluid method within OpenFOAM, Numer. Heat Transf., Part A, Appl. 56 (2009) 631–646.

[19] M. Magnini, B. Pulvirenti, J.R. Thome, Numerical investigation of hydrodynamics and heat transfer of elongated bubbles during flow boiling in a microchannel, Int. J. Heat Mass Transf. 59 (2013) 451–471.

[20] G. Son, V. Dhir, N. Ramanujapu, Dynamics and heat transfer associated with a single bubble during nucleate boiling on a horizontal surface, J. Heat Transf. 121 (1999) 623–631.

[21] S. Tanguy, T. Ménard, A. Berlemont, A level set method for vaporizing two-phase flows, J. Comput. Phys. 221 (2007) 837–853.

[22] S. Tanguy, M. Sagan, B. Lalanne, F. Couderc, C. Colin, Benchmarks and numerical methods for the simulation of boiling flows, J. Comput. Phys. 264 (2014) 1–22.

[23] L.R. Villegas, R. Alis, M. Lepilliez, S. Tanguy, A ghost fluid/level set method for boiling flows and liquid evaporation: application to the Leidenfrost effect, J. Comput. Phys. 316 (2016) 789–813.

[24] J. Schlottke, B. Weigand, Direct numerical simulation of evaporating droplets, J. Comput. Phys. 227 (2008) 5215–5237.

[25] C. Ma, D. Bothe, Numerical modeling of thermocapillary two-phase flows with evaporation using a two-scalar approach for heat transfer, J. Comput. Phys. 233 (2013) 552–573.

[26] A. Esmaeeli, G. Tryggvason, Computations of film boiling. Part I: numerical method, Int. J. Heat Mass Transf. 47 (2004) 5451–5461.

[27] A. Esmaeeli, G. Tryggvason, A front tracking method for computations of boiling in complex geometries, Int. J. Multiph. Flow 30 (2004) 1037–1050.

[28] Y. Sato, B. Ničeno, A sharp-interface phase change model for a mass-conservative interface tracking method, J. Comput. Phys. 249 (2013) 127–161.

[29] Y.-Y. Tsui, S.-W. Lin, Three-dimensional modeling of fluid dynamics and heat transfer for two-fluid or phase change flows, Int. J. Heat Mass Transf. 93 (2016) 337–348.

[30] M.W. Akhtar, S.J. Kleis, Boiling flow simulations on adaptive octree grids, Int. J. Multiph. Flow 53 (2013) 88–99.

[31] Y.-Y. Tsui, S.-W. Lin, Y.-N. Lai, F.-C. Wu, Phase change calculations for film boiling flows, Int. J. Heat Mass Transf. 70 (2014) 745–757.

[32] X.-Y. Luo, M.-J. Ni, A. Ying, M. Abdou, Numerical modeling for multiphase incompressible flow with phase change, Numer. Heat Transf., Part B, Fundam. 48 (2005) 425–444.

[33] R.P. Fedkiw, T. Aslam, B. Merriman, S. Osher, A non-oscillatory Eulerian approach to interfaces in multimaterial flows (the ghost fluid method), J. Comput. Phys. 152 (1999) 457–492.

[34] X.-D. Liu, R.P. Fedkiw, M. Kang, A boundary condition capturing method for Poisson's equation on irregular domains, J. Comput. Phys. 160 (2000) 151–178.

[35] B. Van Poppel, O. Desjardins, J. Daily, A ghost fluid, level set methodology for simulating multiphase electrohydrodynamic flows with application to liquid fuel injection, J. Comput. Phys. 229 (2010) 7977–7996.

[36] S. Kang, Dielectrophoretic motion of two particles with diverse sets of the electric conductivity under a uniform electric field, Comput. Fluids 105 (2014) 231–243.

[37] D. Juric, G. Tryggvason, Computations of boiling flows, Int. J. Multiph. Flow 24 (1998) 387–410.

[38] W.J. Rider, D.B. Kothe, Reconstructing volume tracking, J. Comput. Phys. 141 (1998) 112–152.

[39] D. Gueyffier, J. Li, A. Nadim, R. Scardovelli, S. Zaleski, Volume-of-fluid interface tracking with smoothed surface stress methods for three-dimensional flows, J. Comput. Phys. 152 (1999) 423–456.

[40] B. Lalanne, L.R. Villegas, S. Tanguy, F. Risso, On the computation of viscous terms for incompressible two-phase flows with level set/ghost fluid method, J. Comput. Phys. 301 (2015) 289–307.

[41] M.-J. Ni, R. Munipalli, P. Huang, N.B. Morley, M.A. Abdou, A current density conservative scheme for incompressible MHD flows at a low magnetic Reynolds number. Part II: on an arbitrary collocated mesh, J. Comput. Phys. 227 (2007) 205–228.

[42] H. Johansen, P. Colella, A Cartesian grid embedded boundary method for Poisson's equation on irregular domains, J. Comput. Phys. 147 (1998) 60–85.

[43] D. Calhoun, R.J. LeVeque, A Cartesian grid finite-volume method for the advection–diffusion equation in irregular geometries, J. Comput. Phys. 157 (2000) 143–180.

[44] H. Ji, F.-S. Lien, E. Yee, An efficient second-order accurate cut-cell method for solving the variable coefficient Poisson equation with jump conditions on irregular domains, Int. J. Numer. Methods Fluids 52 (2006) 723–748.

[45] S. Popinet, Gerris: a tree-based adaptive solver for the incompressible Euler equations in complex geometries, J. Comput. Phys. 190 (2003) 572–600.

[46] M.-J. Ni, J.-F. Li, A consistent and conservative scheme for incompressible MHD flows at a low magnetic Reynolds number. Part III: on a staggered mesh, J. Comput. Phys. 231 (2012) 281–298.

[47] V. Alexiades, Mathematical Modeling of Melting and Freezing Processes, CRC Press, 1992.
[48] M.-J. Ni, Consistent projection methods for variable density incompressible Navier–Stokes equations with continuous surface forces on a rectangular collocated mesh, J. Comput. Phys. 228 (2009) 6938–6956.
[49] L. Scriven, On the dynamics of phase growth, Chem. Eng. Sci. 10 (1–2) (1959) 1–13.
[50] M.S. Lee, A. Riaz, V. Aute, Direct numerical simulation of incompressible multiphase flow with phase change, J. Comput. Phys. 344 (2017) 381–418.
[51] L. Florschuetz, C. Henry, A.R. Khan, Growth rates of free vapor bubbles in liquids at uniform superheats under normal and zero gravity conditions, Int. J. Heat Mass Transf. 12 (11) (1969) 1465–1489.
[52] A. Badillo, Quantitative phase-field modeling for boiling phenomena, Phys. Rev. E 86 (4) (2012) 041603.
[53] B. Nath, G. Biswas, A. Dalal, K.C. Sahu, Cross-stream migration of drops suspended in Poiseuille flow in the presence of an electric field, Phys. Rev. E 97 (6) (2018) 063106.
[54] S.W. Welch, J. Wilson, A volume of fluid based method for fluid flows with phase change, J. Comput. Phys. 160 (2000) 662–682.
[55] F. Gibou, L. Chen, D. Nguyen, S. Banerjee, A level set based sharp interface method for the multiphase incompressible Navier–Stokes equations with phase change, J. Comput. Phys. 222 (2007) 536–555.
[56] D.-Z. Guo, D.-L. Sun, Z.-Y. Li, W.-Q. Tao, Phase change heat transfer simulation for boiling bubbles arising from a vapor film by the VOSET method, Numer. Heat Transf., Part A, Appl. 59 (2011) 857–881.
[57] V. Klimenko, Film boiling on a horizontal plate—new correlation, Int. J. Heat Mass Transf. 24 (1981) 69–79.
[58] Y.-J. Lao, R.E. Barry, R.E. Balzhiser, A study of film boiling on a horizontal plate, in: International Heat Transfer Conference 4, vol. 24, Begel House Inc., 1970.
[59] P. Davidson, Magnetic damping of jets and vortices, J. Fluid Mech. 299 (1995) 153–186.
[60] J. Sommeria, R. Moreau, Why, how, and when, MHD turbulence becomes two-dimensional, J. Fluid Mech. 118 (1982) 507–518.